



# Ca<sup>2+</sup> and Ag<sup>+</sup> orient low-molecular weight amphiphile self-assembly into “nano-fishnet” fibrillar hydrogels with unusual $\beta$ -sheet-like raft domains

Alexandre Poirier, Patrick Le Griel, Ingo Hoffmann, Javier Perez, Petra Pernot, Jérôme Fresnais, Niki Baccile

## ► To cite this version:

Alexandre Poirier, Patrick Le Griel, Ingo Hoffmann, Javier Perez, Petra Pernot, et al.. Ca<sup>2+</sup> and Ag<sup>+</sup> orient low-molecular weight amphiphile self-assembly into “nano-fishnet” fibrillar hydrogels with unusual  $\beta$ -sheet-like raft domains. *Soft Matter*, 2023, 19 (378 - 393), 10.1039/D2SM01218A . hal-03576359v2

**HAL Id: hal-03576359**

**<https://hal.science/hal-03576359v2>**

Submitted on 15 Dec 2022

**HAL** is a multi-disciplinary open access archive for the deposit and dissemination of scientific research documents, whether they are published or not. The documents may come from teaching and research institutions in France or abroad, or from public or private research centers.

L'archive ouverte pluridisciplinaire **HAL**, est destinée au dépôt et à la diffusion de documents scientifiques de niveau recherche, publiés ou non, émanant des établissements d'enseignement et de recherche français ou étrangers, des laboratoires publics ou privés.

# **Ca<sup>2+</sup> and Ag<sup>+</sup> orient low-molecular weight amphiphile self-assembly into “nano-fishnet” fibrillar hydrogels with unusual $\beta$ -sheet-like raft domains**

Alexandre Poirier,<sup>a</sup> Patrick Le Griel,<sup>a</sup> Ingo Hoffmann,<sup>b</sup> Javier Perez,<sup>c</sup> Petra Pernot,<sup>d</sup> Jérôme Fresnais,<sup>e</sup> Niki Baccile<sup>a,\*</sup>

<sup>a</sup> Sorbonne Université, Centre National de la Recherche Scientifique, Laboratoire de Chimie de la Matière Condensée de Paris, LCMCP, F-75005 Paris, France

<sup>b</sup> Institut Laue-Langevin, 38042 Grenoble, France

<sup>c</sup> Synchrotron Soleil, L'Orme des Merisiers, Saint-Aubin, BP48, 91192 Gif-sur-Yvette Cedex, France

<sup>d</sup> ESRF – The European Synchrotron, CS40220, 38043 Grenoble, France

<sup>e</sup> Sorbonne Université, CNRS, Laboratoire de Physico-chimie des Électrolytes et Nanosystèmes Interfaciaux, PHENIX - UMR 8234, F-75252, Paris Cedex 05, France

\* Corresponding author:

Dr. Niki Baccile

E-mail address: niki.baccile@sorbonne-universite.fr

Phone: +33 1 44 27 56 77

## **Abstract**

Low-molecular weight gelators (LMWG) are small molecules ( $M_w < \sim 1$  kDa), which form self-assembled fibrillar networks (SAFiN) hydrogels in water triggered by an external stimulus. The great majority of SAFiN gels is described by an entangled network of self-assembled fibers, in analogy to a polymer in a good solvent. In some rare cases, a combination of attractive Van der Waals and repulsive electrostatic forces drives the formation of bundles having a suprafibrillar hexagonal order. In this work, an unexpected micelle-to-fiber transition is triggered by Ca<sup>2+</sup> or Ag<sup>+</sup> ions added to a micellar solution of a novel glycolipid surfactant, whereas salt-induced fibrillation is not common for surfactants. The resulting SAFiN, which forms hydrogel above 0.5 wt%, has a “nano-fishnet” structure, characterized by a fibrous network of both entangled fibers and  $\beta$ -sheets-like rafts, generally observed for silk fibroin, actin hydrogels or mineral imogolite nanotubes, but not known for SAFiN. The  $\beta$ -sheets-like raft domains are characterized by a combination of cryo-TEM and SAXS and seem to contribute

to the stability of the glycolipid gels. Furthermore, the glycolipid is obtained by fermentation from natural resources (glucose, rapeseed oil), thus showing that naturally-engineered compounds can have unprecedented properties, when compared to the wide range of chemically derived amphiphiles.

## Introduction

Water thickening in hydrogels is generally produced by an entangled fibrous network of polymers, chemically or physically cross-linked,<sup>1,2</sup> giving rise to widespread consumer products.<sup>3</sup> To improve the biocompatibility, biopolymer-based hydrogels became a source of interest and a number of studies nowadays exist in this field.<sup>4</sup> However, the gelling process by polymers is often irreversible, reason why low molecular weight gelators (LMWG) are developed, for they combine a fascinating self-assembly behavior, driven by non-covalent interactions, and a supramolecular assembly process, which can be tuned<sup>5-8</sup> more or less reversibly to form a gel.<sup>9-11</sup> However, may they be polymeric or self-assembled fibrillar networks (SAFiN), physical gels share the same entangled fibrillar structure.

More peculiar, some biopolymers, like silk fibroin<sup>12-15</sup> or actin<sup>16-18</sup>, have a more complex hydrogel structure, where entanglement coexists with crystalline  $\beta$ -sheet domains, and these constituting junctions of the intertwined fibrillar network. Hydrogels of which the structure combines entanglement and  $\beta$ -sheet domains are referred to have a “nano-fishnet” structure.<sup>12-18</sup>  $\beta$ -sheets, stabilized by a combination of hydrophobic effect and inter-chain hydrogen bonding, provide an important element of structural stability of the gel,<sup>13</sup> of which the network elasticity is related to  $\beta$ -sheet junctions.<sup>12-18</sup> Silk fibroin gels, for instance, are irreversible and stable against temperature,<sup>19</sup> and can only be disassembled with highly concentrated solutions of lithium thiocyanate.

“Nano-fishnet” hydrogels are not classical for SAFiN prepared from amphiphiles, which, at rest, are generally described as physically entangled networks without any long-range organization of the fibers. As a matter of fact, their typical X-ray (or neutron) scattering profile is characterized by the lone form factor of the fibers<sup>20-24</sup> (a more extensive list of references is given in Table S 1). In some rare cases, fibers with a homogeneous distribution of charges around their cross-section show bundling into a columnar phase with hexagonal order (Table S 1).<sup>25,26</sup> To the best of our knowledge, Weingarten *et al.* were one of the few, if not the only ones, showing a lamellar supramolecular arrangement of fibers composed of perylene amphiphiles.<sup>27</sup> However, such arrangement was not associated with the gel but rather to the

colloidal structure before gelling, making it different than typical “nano-fishnet” gels, reported for silk fibroin.<sup>12–18</sup>

In this work, we report the formation of SAFiN amphiphile hydrogels having a “nano-fishnet” structure. The “nano-fishnet” is intended here as a network, where fibers are both entangled and associated side-by-side into structures with lamellar periodicity. The latter have a similar structure to  $\beta$ -sheet domains, defined as short regions in proteins where the polypeptide chain aligns adjacently, or rafts in imogolites,<sup>28</sup> and for this reason they are referred hereafter to as  $\beta$ -sheet-like rafts. The SAFiN hydrogels are only composed of a C18:1 glycolipid (G-C18:1, Figure 1). G-C18:1 was recently discovered through a microbial fermentation process from rapeseed oil.<sup>29</sup> It is characterized by a glucose moiety linked through an acetal bond to the C17 of oleic acid. G-C18:1 does not contain any aminoacid, thus belonging to the family of low molecular weight glycolipid amphiphiles and not to peptides, or proteins.

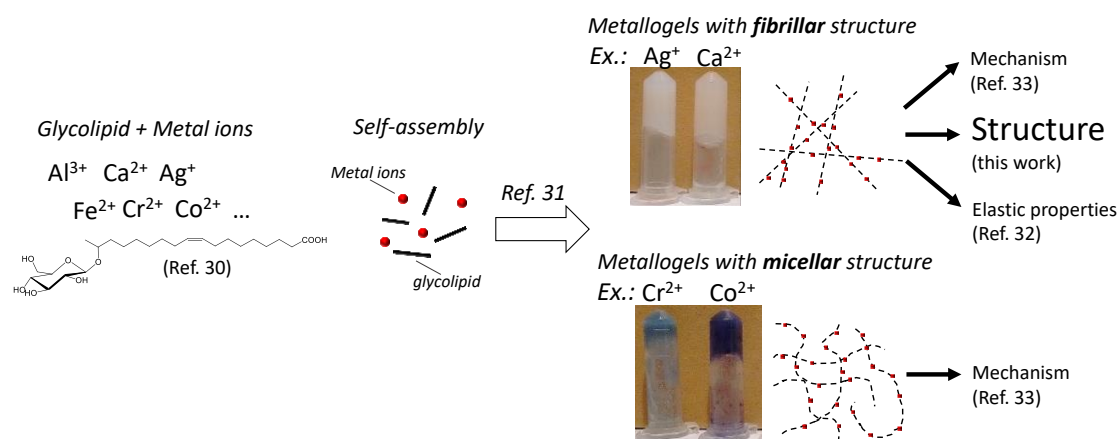


**Figure 1 – G-C18:1 bolaform glycolipid amphiphile<sup>30</sup> and its cation-induced metallogelation.<sup>31</sup> The “nano-fishnet” structure of G-C18:1 fibrillar gels is reported in this work, while the mechanism of formation and their elastic properties are reported elsewhere.<sup>32,33</sup> The mechanism of formation of micellar gels are studied in Ref. <sup>33</sup>.**

Ongoing research has shown that G-C18:1 displays a rare triple surfactant-lipid-gelator nature at concentrations below 5 wt%.<sup>30</sup> Early studies have shown its micellar phase at basic pH and a vesicle phase below neutral pH.<sup>34,35</sup> However, current work<sup>31</sup> shows that addition of specific cations to the micellar phase under neutral-alkaline conditions of pH not only promote a cylinder/wormlike phase, expected for surfactant micelles in contact with multivalent cations,<sup>36–39</sup> but also an unexpected fiber phase<sup>31</sup> able to form SAFiN hydrogels (Figure 1).<sup>32</sup> Self-assembled fibrillar gels are generally reported for peptide, peptide amphiphiles and other LMWG, but not known for anionic surfactants, which tend to form micellar gels when mixed with cations.<sup>40–45</sup>

In this work, the combination of cryogenic transmission electron microscopy (cryo-TEM), which preserves hydration, and small-angle X-ray scattering (SAXS), which, associated to cryo-TEM, guarantees good statistics, demonstrates the formation of fibers, which, in the absence of external shear, organize themselves in a “nano-fishnet” structure. Isothermal titration calorimetry (ITC) and  $^{13}\text{C}$  solid-state nuclear magnetic resonance suggest a multiple role of the cations, involving coordination of G-C18:1 molecules and driving the two-dimensional alignment of the fibers. These hypotheses are consolidated by mechanistic data recorded by mean of *in situ* SAXS experiments and presented elsewhere.<sup>33</sup> In analogy to silk fibroin hydrogels,<sup>19</sup> the “nano-fishnet” organization of G-C18:1, practically unknown in amphiphiles (Table S 1), seems to play a role in the very good stability of G-C18:1 gels against shear and temperature.<sup>32</sup>

## Material and methods

**Chemicals.** The monounsaturated glucolipid G-C18:1 ( $M_w = 460 \text{ g.mol}^{-1}$ ) contains a  $\beta$ -D-glucose unit covalently linked to oleic acid. The molecule is obtained by fermentation from the yeast *Starmerella bombicola* (*AugtB1*) according to the protocol given before.<sup>29,35</sup> The compound is purchased from the Bio Base Europe Pilot Plant, Gent, Belgium, lot N° APS F06/F07, Inv96/98/99 and used as such. According to the specification sheet provided by the producer, the batch (99.4% dry matter) is composed of 99.5% of G-C18:1, according to HPLC-ELSD chromatography data. NMR analysis of the same compound (different batch) was performed elsewhere.<sup>34</sup> NaOH ( $\geq 98\text{wt}\%$  pellets) is purchased from Sigma Aldrich,  $\text{CaCl}_2$  in pellets and liquid 35wt% HCl are purchased from VWR.  $\text{AgNO}_3$  is purchased from Sigma Aldrich.

**Sample preparation.** G-C18:1 is dispersed in milli-Q water and the pH is adjusted by an initial addition of concentrated NaOH (5 M), followed by a refinement with few  $\mu\text{L}$  of more diluted NaOH (or HCl) solution (1 M, 0.5 M or 0.1 M). The targeted molecular ratio to be roughly in the region of pH 8 is  $[\text{NaOH}]/[\text{G-C18:1}] = 0.7\text{-}0.8$ . The solution is homogenized by vortexing. To form a hydrogel, a  $\text{CaCl}_2$ , or  $\text{AgNO}_3$ , solutions are prepared at 1 M and the appropriate amount is added to the G-C18:1 solution according to the molar ratio  $[\text{AgNO}_3]/[\text{G-C18:1}] = 1.0$  and  $[\text{CaCl}_2]/[\text{G-C18:1}] = 0.6$ . Typically, for a total 1 mL volume, 62.5  $\mu\text{L}$  of  $\text{AgNO}_3$  (1 M), or 40  $\mu\text{L}$  of  $\text{CaCl}_2$  (1 M), are added to the complementary volume of 3 wt% G-C18:1. After the addition, the solution is immediately stirred during about 30 s. All samples are

aged between few minutes and 3 days before any experiments. Hydrogels prepared from  $\text{Ca}^{2+}$  and  $\text{Ag}^+$  are respectively labeled  $\{\text{Ca}^{2+}\}\text{G-C18:1}$  and  $\{\text{Ag}^+\}\text{G-C18:1}$ .

Additional information on the experimental methods and analytical techniques are given in the supporting information.

## Results

### *Gelling of glucolipid G-C18:1*

Bolaform glucolipid G-C18:1 contains a free-standing carboxylic acid end-group on its alkyl chain.<sup>30</sup> For this reason, it behaves as a surfactant above and as a lipid below neutrality of water (pH  $\sim 7$ ) and room temperature: a predominant micellar phase is observed at the basic pH while a vesicular phase is reported at acidic pH.<sup>34,35</sup> Qualitative experiments show that precipitation occurs when various sources of cations are added below neutrality, in the vesicle phase, most likely inducing the formation of a lamellar aggregate, in analogy to the effect of lowering pH below 4<sup>46,47</sup> and in agreement with other vesicle-cation systems.<sup>48</sup> On the contrary, adding alkaline earth and transition metal cations in the micellar phase above neutrality induces gelling (Figure 1), as shown by small amplitude oscillatory rheology experiments.<sup>31,32</sup> Previous work<sup>31,33</sup> has shown that the structure of the metallogels is micellar wormlike for those metal ions with complex speciation in water and fibrillar for free metal ions below pH 10. In the latter category,  $\text{Ca}^{2+}$  and  $\text{Ag}^+$  provided the most stable gels, with particular stability towards temperature.<sup>32</sup> The investigation of the gel morphology and the structural role of  $\text{Ca}^{2+}$  and  $\text{Ag}^+$  is then critical to better understand and control the gel properties of the bolaform glucolipid.

The gel properties of both  $\{\text{Ca}^{2+}\}\text{G-C18:1}$  and  $\{\text{Ag}^+\}\text{G-C18:1}$  are determined in the linear viscoelastic regime ( $\gamma = 0.1\%$ ) by frequency sweep experiments at selected  $[\text{X}^+]/[\text{G-C18:1}]$  ratios (Figure 2a,b),  $[\text{X}^+]$  being the molar concentration of the positive charges, taken as  $2[\text{Ca}^{2+}]$  and  $[\text{Ag}^+]$  for  $\text{Ca}^{2+}$  or  $\text{Ag}^+$ , respectively. Results show that  $G' > G''$  by at least one order of magnitude, thus confirming the gel behaviour of the materials. Additionally, Figure 2c shows the increase of  $G'$  against the G-C18:1 weight fraction,  $\phi_{\text{G-C18:1}}$ , at a fixed  $[\text{cation}]/[\text{G-C18:1}]$  ratio, which is optimized and discussed elsewhere.<sup>31,32</sup> One finds that silver hydrogels are at least one order of magnitude stronger than calcium gels.  $G'$  scales with  $\phi_{\text{G-C18:1}}$  following a power law of 2.3 and 2.6 for calcium and silver hydrogels, respectively. Scaling law with a power dependency between 2.3 and 2.6 are close to 2.25, the well-known value reported for entangled fibrils in a good solvent, according scaling theory developed by De Gennes in 1976.<sup>49</sup> Similar values are also reported for nanofibrillated systems,<sup>50</sup> including SAFiN hydrogels.<sup>51</sup>

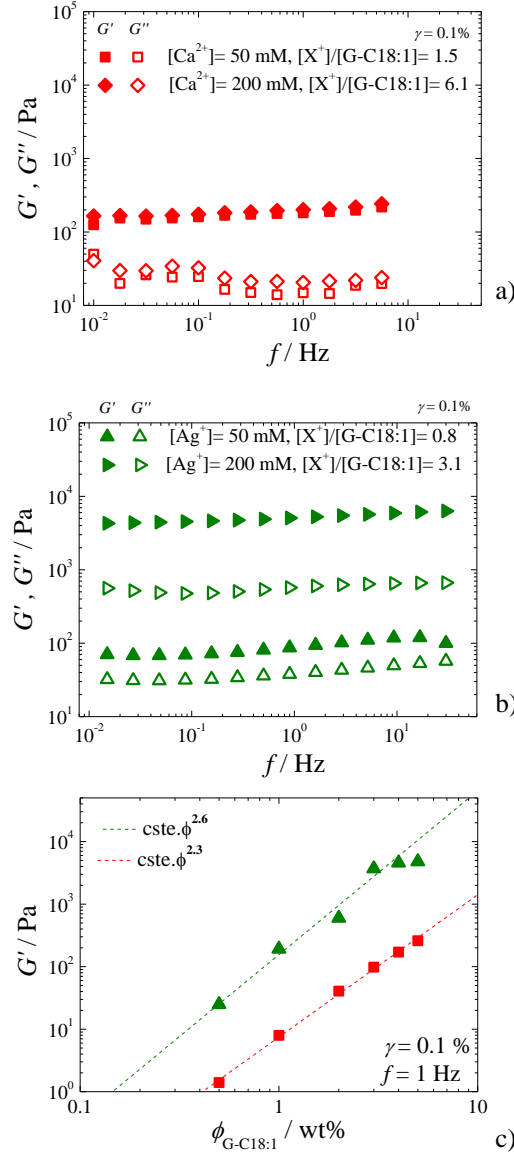


**Figure 2 – Oscillatory rheology.** Frequency-dependent elastic and viscous moduli,  $G'$  and  $G''$ , of a)  $\{Ca^{2+}\}G-C18:1$  (red square) or b)  $\{Ag^+\}G-C18:1$  (green triangle) hydrogels ( $\phi_{G-C18:1} = 3$  wt%, basic pH). Ion concentrations in the lipid solution are 50 mM and 200 mM. c) Elastic moduli,  $G'$ , of  $\{Ca^{2+}\}G-C18:1$  (square) and  $\{Ag^+\}G-C18:1$  (triangle) hydrogels at basic pH as a function of G-C18:1 weight fraction,  $\phi_{G-C18:1}$ , at the molar ratio  $[Ca^{2+}]/[G-C18:1] = 0.6$  and  $[Ag^+]/[G-C18:1] = 1$ . The dash lines correspond to a linear power law fitting. Additional data and corresponding frequency and strain sweep profiles are given in Ref. <sup>32</sup>.

Gelling of glucolipid G-C18:1 is unexpected. Its known phase behavior<sup>34,35</sup> cannot explain its gelling properties. Considering its tendency to form interdigitated membranes at pH below 7, one could suppose the formation of vesicle gels,<sup>52</sup> or even a lamellar gel,<sup>53</sup> in analogy with the gelling properties of a similar glucolipid with a saturated fatty acid.<sup>54</sup> A simplistic understanding of the cations effect on self-assembly, well known in the literature,<sup>41,44,55,56</sup> could suppose neutralization of the negative charges of G-C18:1. Consequent variation in the lipid

packing parameter could lead to the formation of either defective membranes, responsible for gelling in lipid lamellar systems,<sup>53,54</sup> or elongated (cylinder or wormlike) micelles.<sup>36–39,45,57–59</sup> However, a combination of cryo-TEM and SAXS experiments do not corroborate these hypotheses, whereas combination of these techniques is critical, because cryo-TEM preserves sample hydration, while solution SAXS confirms cryo microscopy data with good statistics.

#### *“Nano-fishnet” structure of G-C18:1 gels*

Cryo-TEM (Figure 3) and SAXS (Figure 4) of  $\{\text{Ca}^{2+}\}\text{G-C18:1}$  and  $\{\text{Ag}^+\}\text{G-C18:1}$  hydrogels invalidate the lamellar and micellar hypotheses in favour of a fibrillar phase, never reported before for this compound and actually not expected for anionic surfactants solutions in the presence of mono or multivalent cations (for a broader literature survey, refer to ref. <sup>31</sup>). Previous cryo-TEM and SAXS analysis of a salt free G-C18:1 solution show either free micelles, membranes or vesicles at pH above 8, around 7 and below 7, respectively.<sup>34</sup>

Free fibers (Figure 3, panels b and 1) but also fiber di/trimers (Figure 3, panels e,f and 3-6) and even  $\beta$ -sheet-like rafts (Figure 3a,c,d) are observed throughout the sample, both for  $\{\text{Ca}^{2+}\}\text{G-C18:1}$  and  $\{\text{Ag}^+\}\text{G-C18:1}$  hydrogels. The width of the individual fiber is estimated to about  $10 \pm 1$  nm for  $\{\text{Ca}^{2+}\}\text{G-C18:1}$  and  $5 \pm 1$  for  $\{\text{Ag}^+\}\text{G-C18:1}$ . As far as the morphology is concerned, cryo-TEM may erroneously suggest the presence of nanotubes. However, a more attentive observation shows that what look like nanotubes (e.g., Figure 3d) are in fact an association of individual fibers over hundreds of nanometers, or even micron, scale. This is particularly clear on Figure 3, panels 3-6 for the  $\{\text{Ag}^+\}\text{G-C18:1}$ : individual fibers merge at a given point in space and are associated for their entire length. Figure 3, panel 3 nicely shows how a single flexible fiber connects two other individual fibers and their extremities.

Cryo-TEM then suggests specific attractive side-by-side interactions between the fibers, spontaneously occurring in water in the absence of shearing. Interactions, of which the possible driving force is discussed later, occur on length scales of tens of nanometers and seem to drive the lateral association of the fibers into flat structures with periodic order. These are reminiscent of rafts, as occasionally found in imogolites (mineral aluminosilicates).<sup>28</sup> However, in that case, the analogy to *log rafts* was justified by the fact that imogolites are in the shape of nanotubes. On the other hand, the ordered flat structures in Figure 3 recall  $\beta$ -sheets, a common motif in the secondary structure of proteins. If  $\beta$ -sheets are, by definition, associated to (complex) macromolecules only, the terminology  $\beta$ -sheet-like structure can be employed here in a broader sense to non-macromolecular systems, like aminoacid-free low molecular weight amphiphiles, assembling into rafts of flat fibers.



Given the above, and in analogy to the “nano-fishnet” structure described for silk fibroin<sup>12-15</sup> and actin<sup>16-18</sup> gels, the lateral association of G-C18:1 fibers in its gel phase will be addressed to as  $\beta$ -sheet-like rafts. These are uncommon in amphiphile SAFIN,<sup>27</sup> and, to the best of our knowledge, not reported for amphiphile SAFIN hydrogels (an extensive literature survey given in Table S 1), which are generally characterized either by entanglement or by hexagonally packed bundles, if fibers are charged.<sup>25,26</sup>

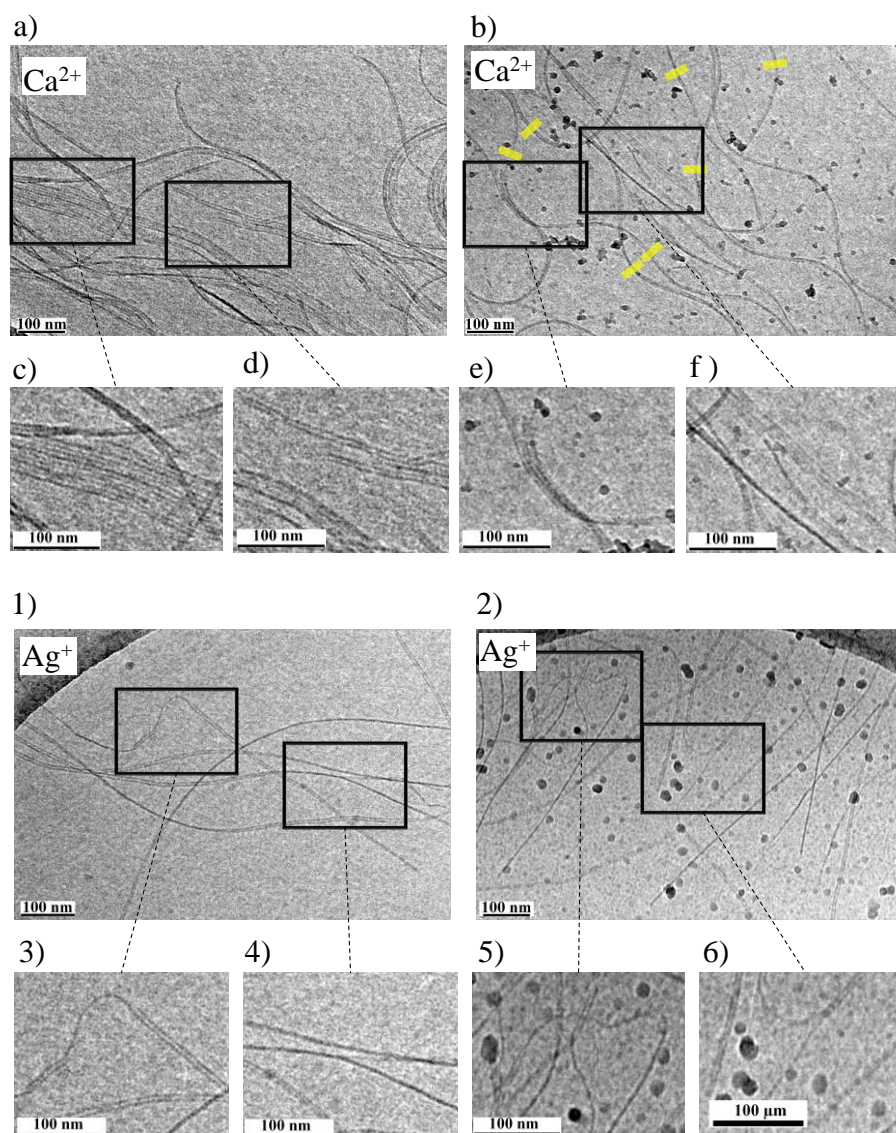


**Figure 3 - Cryo-TEM images of 0.5 wt% G-C18:1 at a ratio  $[\text{Ca}^{2+}]/[\text{G-C18:1}] = 0.6$  (a-f),  $[\text{Ag}^+]/[\text{G-C18:1}] = 1$  (1-6) in water at a basic pH. Samples are not sheared. In a,b) and 1,2) black rectangles indicate magnified regions of interest. a) Large ordered rafts, magnified in c, d). b) Free fibrils locally assembled into dimeric or trimeric rafts. Yellow lines are used to measure the fiber's cross section,  $10.3 \pm 0.8$  nm. Magnified picture e,f) show local and small rafts. 1,2) Fibrils from  $\text{Ag}^+$ -containing sample locally self-assemble in small dimeric rafts, magnified in 3-6).**

Both the fibrillar structure and massive supra-fibrillar organization in bulk are confirmed by SAXS (Figure 4). The overall signal of the ion-free liquid G-C18:1 solution at basic pH

(black line, Figure 4a) is consistent with the coexistence of two or more species, attributed to micelles and flat membranes during the pH-induced micelles-to-vesicle transition for this sample in the pH range between 7 and 8.<sup>34,35</sup> The broad hump centered at about  $0.8 \text{ nm}^{-1}$  and the oscillation above  $1 \text{ nm}^{-1}$  are characteristics of repulsive electrostatic interactions and micellar morphology, respectively. The strong low- $q$  scattering, with  $\log(I)$ - $\log(q)$  dependency of about -2, is typical for flat structures.<sup>34,35</sup> When a gel forms by adding the appropriate amount of  $\text{Ca}^{2+}$  (or  $\text{Ag}^+$ ), the micelle signal is replaced by a more complex scattering profile having a -2 dependency of the intensity below  $0.4 \text{ nm}^{-1}$  and a series of diffraction peaks above  $0.5 \text{ nm}^{-1}$  and attributed to a long-range structural order.

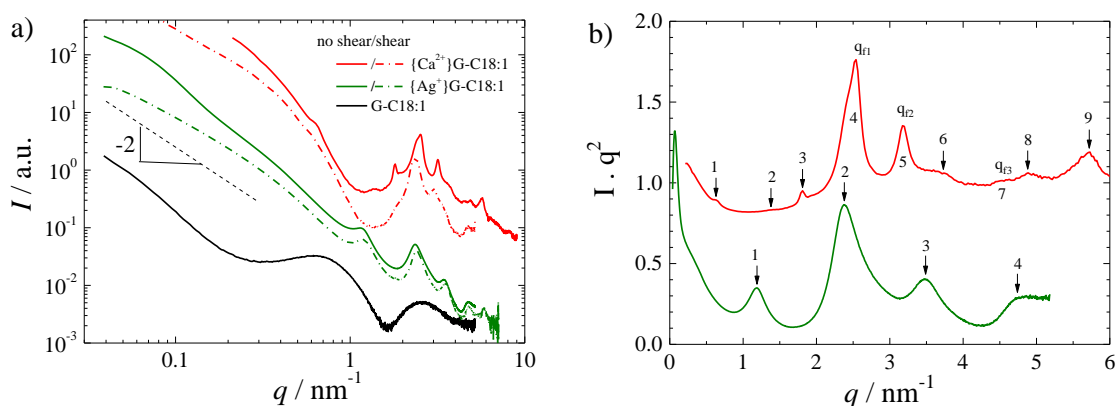


**Figure 4 - SAXS profiles of a) 2 wt% of G-C18:1 in water at a basic pH (pH 8) in the absence (black) and presence of  $\text{Ca}^{2+}$  (red) and  $\text{Ag}^+$  (green). Segmented lines: sheared gels; straight lines: static gels. b) Kratky plots of static gels in a). Peaks are listed in Table S 2 of the supporting information.**

All  $\{\text{Ag}^+\}$ G-C18:1 gels have the same SAXS profile, independently of the G-C18:1 concentration (Figure S 1b), content of  $\text{Ag}^+$  or shearing (Figure 4a). Four broad peaks at a ratio of 1:2:3:4 (Figure 4b, Table S 2b) identify a lamellar order. Since cryo-TEM excludes any flat lamellar phase, as previously observed for analogous compounds,<sup>34</sup> and it only shows individual fibers and their lateral association, the lamellar order can only be explained by the side-by-side association of the fibers. The first peak is systematically observed at  $1.18 \text{ nm}^{-1}$ , corresponding to a repeating distance of  $5.32 \text{ nm}$ , which includes the fiber's cross section and interfiber water layer. The latter is estimated to few Å according to cryo-TEM, that is in the range of the primary hydration force counter balancing attractive force of Van der Waals contributions between fibers.<sup>60</sup> A fiber's cross-section in the order of  $5 \text{ nm}$  is then in good agreement with the qualitative estimation of the fibers' lateral dimension by cryo-TEM. The low- $q$  slope of the SAXS profiles corresponding to this set of samples is hard to evaluate due to the superposition of two scattering signals below and above  $0.1 \text{ nm}^{-1}$ . Tentative simulation

of the {Ag<sup>+</sup>}G-C18:1 SAXS profiles corresponding to the 0.1 wt% and 3 wt% samples (Figure S 1e) confirms the need of two models, as the use of a single model does not allow to simulate the entire SAXS curve. A parallelepiped model accounts for the scattering of individual fibers in the mid-q/high-q range, and a lamellar pseudo-crystal model accounts both for the scattering of the rafts at low-q and the lamellar peaks at high-q. Details of the modelling strategy are given in Table S 3 and on Page S8-S10 of the Supporting Information.

{Ca<sup>2+</sup>}G-C18:1 gels display two systematic SAXS profiles. Sheared gels, may they be obtained by controlled shear<sup>32</sup> or by the simple action of introducing them in the SAXS capillary, show the same scattering-diffraction pattern, typically illustrated by the segmented red line in Figure 4a, and independently of the lipid concentration (Figure S 1a). The low-q scattering has a log(I)-log(q) dependence between -1.8 and -2, observed before for fibers with a flat cross-section.<sup>61,62</sup> Four diffraction peaks are also observed and they are most likely associated with the fiber's crystalline structure, tentatively attributed to an oblique lattice within the fiber's plane (Figure S 2a) and discussed in more details in the Supporting Information (Figure S 2 and discussion Page S11-S12).

{Ca<sup>2+</sup>}G-C18:1 gels at rest generate a scattering profile with a similar low-q slope (-2) but a richer diffraction pattern than the one commented above. A series of additional peaks, starting at  $q = 0.62 \text{ nm}^{-1}$  superpose to the pattern corresponding to the fiber's structure. Indexed from 1 through 9 in the Kratky plot in Figure 4b, they strongly suggest a lamellar order, fully listed in Table S 2a. The peak at  $q = 0.62 \text{ nm}^{-1}$  identifies a typical size of 10.1 nm, in good agreement with the corresponding fiber's cross section estimated by cryo-TEM, and indicating that about four G-C18:1 molecules are contained in the fiber's cross-section, as possibly illustrated in Figure S 2a,b.

The lamellar order found in SAXS for both {Ca<sup>2+</sup>}G-C18:1 and {Ag<sup>+</sup>}G-C18:1 gels cannot be explained by a classical 2D liquid crystalline lamellar phase and it rather confirms the side-by-side association of fibers into  $\beta$ -sheet-like rafts (Figure 3). Interestingly, the width of the SAXS peaks is not equivalent across samples. The peaks are systematically sharper for the {Ca<sup>2+</sup>}G-C18:1 gels than for the {Ag<sup>+</sup>}G-C18:1 gels, probably indicating that {Ca<sup>2+</sup>}G-C18:1 gels are characterized by a fibrillar alignment over a longer distance. Cryo-TEM seems to corroborate this observation showing rafts composed of more than three fibers for {Ca<sup>2+</sup>}G-C18:1 gels (Figure 3c-f), while the association of only two or three fibers are generally observed for {Ag<sup>+</sup>}G-C18:1 gels (Figure 3, panels 3-6).

The dependency of log(I)-log(q) at low scattering vectors (slope) identifies either a specific shape (-1: rod, -2: plane) but also mass (-1 / -3) and surface (-3 / -4) fractals.<sup>63</sup> Figure S 1c

summarizes the slopes measured for the  $\{\text{Ca}^{2+}\}$ G-C18:1 gels analyzed by SAXS. Cylindrical fibers are expected to follow a -1 dependence, but this value is only observed under highly diluted (0.1 wt%) conditions. Upon increasing concentration, the slope systematically increases towards values close to -2, varying between -1.8 for sheared gels and -2.2 for gels at rest. Values in the order of -2 are certainly classical for nanobelts<sup>61,64</sup> and twisted ribbons,<sup>65</sup> and observed before for other glycolipids.<sup>51,62</sup> However, it is not reasonable to explain a concentration-dependent evolution from -1 to an approximate -2 slope by a change in fiber morphology. If an isotropic cross-section of individual fibers themselves is not excluded, and actually highly possible, one could also interpret the -2 slope as the signature of the extensive presence of fiber rafts, flat in nature.  $\{\text{Ag}^+\}$ G-C18:1 gels display a more complex low-q scattering behavior. A crude estimation of the low-q slope shows values between -2.6 and -3, typical of mass fractals. However, a closer look at some profiles (2 wt%, 3 wt% in Figure S 1b or Figure 4) actually indicates the superposition of at least two scattering signals, making it impossible to have a correct estimate of the slope. Occasionally, the scattering profile does not appear multicomposite and typical slopes in the order of -2 can also be measured, reinforcing the hypothesis of flat fibers/rafts.

The above is confirmed by the simulation of the SAXS profiles of  $\{\text{Ca}^{2+}\}$ G-C18:1 and  $\{\text{Ag}^+\}$ G-C18:1 (Figure S 1d,e). In particular,  $\{\text{Ca}^{2+}\}$ G-C18:1 at 0.1 wt% can be modelled with a single parallelepiped model (Figure S 1d), while the sample at 3 wt% requires a second model accounting for the paracrystal structure of the rafts (Figure S 1d, Table S3 and discussion Page S8-S10 in the Supporting Information). As commented above,  $\{\text{Ag}^+\}$ G-C18:1 systematically requires the paracrystal structure model to simulate the SAXS profiles, even at low concentration (0.1 wt%). Even if the simulations could not be optimized with a fitting procedure due to the large number of critical independent parameters (Table S 3), they help understanding the fact that the slope of  $\{\text{Ag}^+\}$ G-C18:1 SAXS curves is far from the value of -2 due to the scattering contributions of both individual fibers and rafts. They also show that rafts composed of few fibers (the value of 5 Nlayers, representing the number of associated fibers, was used in the simulations) already exist in diluted silver solutions. This is not the case for calcium-based fibers.

#### *Origin of the fiber's $\beta$ -sheet-like raft structure*

Fibrillar hydrogels, of which the elastic properties are driven by entanglement, are commonly observed for a large number of systems, including biopolymers,<sup>14</sup> surfactants,<sup>66</sup> peptides<sup>67</sup> and peptide amphiphiles,<sup>10</sup> biosurfactants.<sup>51,68</sup> Fibrillation by mono and multivalent

cations is also well known for bile salts,<sup>69</sup> low-molecular weight gelators,<sup>5,70,71</sup> peptides, peptide-derivatives<sup>41,42,72</sup> and polymers.<sup>73–77</sup> If the magnitude of the elastic modulus varies from system to system and depends on the length, dispersion in size of the fiber's cross section, fibers content, spherulite formation, most amphiphilic systems are characterized by the absence of specific forces driving supra-fibrillar interactions. The corresponding SAXS (or SANS) scattering profiles are characterized by the fiber's form (and possibly structure) factor (see references "SAFiN with disordered fibers" in Table S 1).

Excluding the case of complex proteic or peptidic macromolecules (e.g., silk fibroin, collagen) and in the absence of external driving forces (e.g., magnetic or electric fields, shearing), only a restricted number of amphiphiles shows some supra-fibrillar order, systematically characterized by the formation of bundles having 2D hexagonal packing (references in Table S 1). For instance, amphiphilic peptides assemble into long-range hexagonal packing of fibrils in bulk solution, driven by electrostatic repulsion of the charged aminoacids in the peptide portion.<sup>78</sup> Less defined bundles with a hexagonal packing are also suggested for steroid derivatives.<sup>25</sup> Similar findings, but on microtubules, were reported by Needleman *et al.*<sup>79</sup> As a general understanding, a combination between attractive Van der Waals and repulsive (short-range) hydration and/or (long-range) electrostatic forces can sometimes drive fiber bundling, generally into hexagonal lattice<sup>79,80</sup> (additional references in Table S 1) and rarely into lamellar dehydrated crystals.<sup>81</sup> Such phenomenon is also driven by di- or multivalent counterions, indicating that salt bridge-like cross-linking could be another possible, additional, driving force.<sup>79,80</sup> The work of Terech *et al.* is of particular interest, because it shows the gelling properties of tripodal cholamide-based molecules in relationship to their fibrillation into hexagonally ordered bundles.<sup>25</sup> On the other hand, one of the few works exhibiting lamellar aggregation of self-assembled fibers was only reported to occur in a colloidal solution, but not in the corresponding salt-induced hydrogel.<sup>27</sup>

The present system shows some interesting features with respect to the literature.<sup>30</sup> First of all,  $\text{Ca}^{2+}$  and  $\text{Ag}^+$  drive an unexpected micelle-to-fiber, rather than micelle-to-vesicle or micelle-to-wormlike transition. The latter is not only expected for surfactants-cation systems, but also found for G-C18:1 either upon acidification of pH<sup>34,35</sup> or by employing transition metal cations with complex speciation in water.<sup>31</sup> Besides fibrillar entanglement,  $\beta$ -sheet-like rafts seem to play an important role in the gel strength and fibers' stability under shear and at temperatures as high as 70°C.<sup>32</sup>

On the basis of concentration- and shear-dependent SAXS experiments,  $\text{Ca}^{2+}$  and  $\text{Ag}^+$  play a slightly different role.  $\{\text{Ca}^{2+}\}$ G-C18:1 systematically forms crystalline fiber from low to

high concentrations (Figure S 1). They tend to associate into lamellar rafts at rest (shear/no shear profiles in Figure 4), depicting a two-step mechanism, even if the occasional signature of rafts can be observed under shear or at low concentrations. The corresponding hydrogel is less stable against temperature<sup>32</sup> while the rafts disassemble under shear. On the contrary, {Ag<sup>+</sup>}G-C18:1 immediately forms fiber rafts in a single step, independently from concentration (Figure S 1) and shear (Figure 4 and Ref. <sup>32</sup>). Furthermore, gelation by silver occurs at lower  $\phi_{\text{G-C18:1}}$  and G' is at least ten times higher than with calcium (Figure 2). This is probably explained by the coordination effect of carboxylate groups on silver ions, as also suggested by the lack of fibrillation when Na<sup>+</sup> is employed.

Ag<sup>+</sup> is known to form a crystalline structure with a large number of fatty acids by complexation with their COO<sup>-</sup>.<sup>82</sup> Ag<sup>+</sup>/COO<sup>-</sup> interaction has been described for many crystalline complexes.<sup>83,84</sup> However, gels formed by Ag<sup>+</sup>/COO<sup>-</sup> complexes have received less attention if compared to gels based on silver-nitrogen interaction or silver nanoparticles.<sup>5</sup> Metal ion Ag<sup>+</sup> is known to bridge peptides, coordinated by nitrogen<sup>85</sup> and bile salts.<sup>69</sup> Fibrous network based on Ag<sup>+</sup>/COO<sup>-</sup> complex can be obtained in organic solvent by solubilization at high temperature and cooling.<sup>69</sup> In water, polymeric gels induced by Ag<sup>+</sup> bridging carboxylate groups have been described, mainly for the use of silver as an antimicrobial agent.<sup>86</sup> A natural tripeptide was found as a ligand to form a lamellar hydrogel by Ag<sup>+</sup>/sulfur complexation.<sup>87</sup>

The different impact of silver and calcium ions on the self-assembly process of G-C18:1 is nicely corroborated by isothermal titration calorimetry (ITC) experiments, a technique usually employed to characterize the energetic interaction between active sites of molecules, proteins, or more generally binding ligands.<sup>88</sup> It consists in measuring the heat exchanged by a reaction during titration between a titrated molecule by a titrant one.

Figure 5b,c summarize the area per injection versus the molar ratio of the titrations for Ca<sup>2+</sup> and Ag<sup>+</sup>, respectively. For Ca<sup>2+</sup>, the data are consistent with a two-sites binding model, from which the enthalpy of interaction can be extracted for the two steps of interactions, in complement with the corresponding stoichiometries (Table 1).<sup>89</sup> Binding is characterized by an endothermic ( $\Delta H = 6.01$  kJ/mol), typical for non-specific interactions (e.g., hydrophobic effect), and exothermic ( $\Delta H = -11.17$  kJ/mol), typical for specific interactions, process. The corresponding stoichiometric coefficients are 0.1 and 0.3, respectively, and the free energy is comparable (Table 1). For Ag<sup>+</sup>, a classical independent model is used to fit the data, where only one strong exothermic event ( $\Delta H = -37.12$  kJ/mol) is observed during titration, with the stoichiometry of 0.5 and free energy of -25.4 kJ/mol (see Figure S 3 for raw data). ITC shows that two distinct phenomena characterize the Ca<sup>2+</sup> system, of which the enthalpy of reactions is

less exothermic than for  $\text{Ag}^+$ . These results corroborate the difference in terms of structure (this work) and kinetics (Ref. <sup>33</sup>) observed by SAXS, and in particular the strong and immediate reactivity of the  $\text{Ag}^+$  system.

**Table 1 – Thermodynamic parameters extracted from fitting ITC data in Figure 5b,c.**

| Sample                     | Site | $\Delta H$ / kJ/mol | $\Delta S$ / J/mol | $\Delta G$ / kJ/mol | $n$ |
|----------------------------|------|---------------------|--------------------|---------------------|-----|
| {Ca <sup>2+</sup> }G-C18:1 | 1    | 6.01                | 117.3              | -29.2               | 0.1 |
|                            | 2    | -11.17              | 37.37              | -22.4               | 0.3 |
| {Ag <sup>+</sup> }G-C18:1  | -    | -31.95              | -22.00             | -25.4               | 0.5 |

More specifically, the variation of enthalpy and stoichiometry ( $n_1=0.1$ ;  $n_2=0.3$ ) seems to be a proof of a first interaction of the  $\text{Ca}^{2+}$  ions to the G-C18:1, with a secondary cooperative interaction partially hindered by the structuration observed in the fibers. Indeed,  $\Delta H_2$  (-11 kJ/mol) is in fairly good agreement with the absolute values obtained for  $\text{Ca}^{2+}$  adsorption onto alginate (-11.6 kJ/mol for Protanal H120L, Mw= 404 kDa) and low methoxy pectin (-12.1 kJ/mol).<sup>77,90</sup> In fact, the mechanism could be more complex, as shown by the alternate sign of enthalpy variation ( $\Delta H_1 > 0$ ;  $\Delta H_2 < 0$ ).

The most important non-specific endothermic process involved in the self-assembly of amphiphiles or polymers is generally related to the entropic gain in the release of water molecules. The mechanisms behind this phenomenon are multifold. The most important one is probably the well-known hydrophobic effect, known to drive the self-assembly of amphiphiles or polymers,<sup>88,91,92</sup> and actually observed for the interaction between G-C18:1 and polylysine.<sup>46</sup> However, a number of other phenomena are known to be endothermic, such as dehydration due to ion exchange (e.g.,  $\text{Na}^+$  against  $\text{Ca}^{2+}$ ),<sup>92</sup> the weak binding of  $\text{Ca}^{2+}$  to lipid vesicles,<sup>93</sup> micelle-to-rod morphological transitions<sup>94,95</sup> and micellization of zwitterionic surfactants.<sup>91</sup> On the other hand, exothermic process are generally associated with specific interactions, some of which could characterize the self-assembly of {Ca<sup>2+</sup>}G-C18:1: ligand-ion binding (e.g.,  $\text{Ca}^{2+}$ -EDTA),<sup>96</sup> formation of ordered “egg-box” structures in pectin or alginate systems,<sup>77,90</sup> micelle-to-rod morphological transitions<sup>97</sup> and micellization of cationic surfactants.<sup>91</sup>

In the absence of additional data, one can safely state that the addition of calcium induces an initial endothermic, entropic, process. The initial micelle-to-fiber transition in {Ca<sup>2+</sup>}G-C18:1 is certainly driven by the release of water molecules associated with two possibly coexisting phenomena, sodium-calcium ion exchange<sup>92</sup> and the hydrophobic effect related to the structural rearrangement of the fatty acid tails. The latter is driven by the need for two G-C18:1 molecules to neutralize one  $\text{Ca}^{2+}$ . The second exothermic step is most likely related to



ligand-ion binding<sup>92,96</sup> driven by the proximity between  $\text{COO}^-$  and  $\text{Ca}^{2+}$  inside, but also across the fibers, in analogy to the “egg-box” structures.<sup>77,90</sup> The cryo-TEM (Figure 3) and SAXS (Figure 4) data reasonably corroborate the latter interpretation.

It is interesting to note that the stoichiometry is  $n = 0.5$ , instead of 1, for  $\{\text{Ag}^+\}\text{G-C18:1}$ , strongly suggesting a coordination of silver by two carboxylate groups, also found for other systems based on bile salts.<sup>69</sup> One must also depict a slightly deficient,  $n_1 + n_2 = 0.4$ , stoichiometry for  $\{\text{Ca}^{2+}\}\text{G-C18:1}$ , probably explained by defective cations/carboxylates interactions. This can be altered by mixing of the sample inside the measuring cell (250 rpm), which can be a limiting factor that reduces the value of  $n_1$ , compared to the quasi-static assembly of G-C18:1 for the SAXS and rheology measurements. Finally, Figure S 3 compares two ITC titrations, which explore two ranges of molar ratio (0-0.7 and 0-1.1). The second titration implies a more rapid mixing across the stoichiometric values obtained from the former titration ( $n_1 = 0.1$ ;  $n_2 = 0.1$ ). This is in favor of the importance of the kinetics of mixture that allows a more complete interaction between calcium ions and the binding site of G-C18:1, prior to their assembly into fibers.

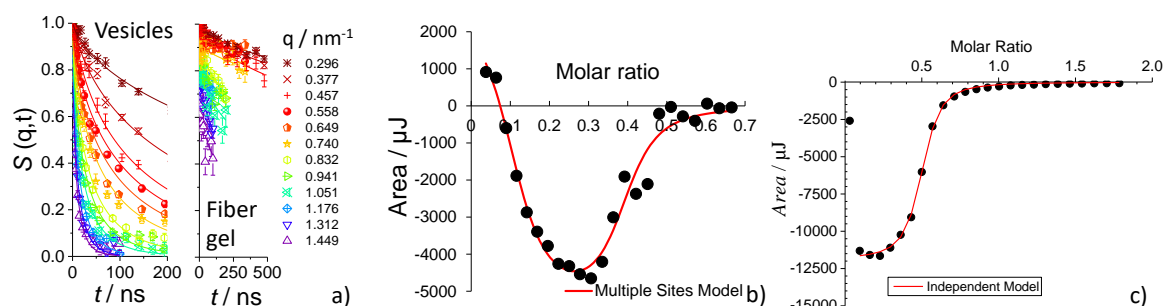


**Figure 5 - a)** Neutron spin-echo (NSE) experiments performed on G-C18:1 vesicles solution at 2 wt% ( $\text{Ca}^{2+}$ -free, pH 6.2) and fibrillar  $\{\text{Ca}^{2+}\}\text{G-C18:1}$  gel ( $[\text{Ca}^{2+}]/[\text{G-C18:1}] = 0.61$ , pH 8). Normalized,  $q$ -dependent, spin-echo intermediate function. Data are fitted with Eq. S1. **b-c)** Isothermal titration calorimetry experiments performed at  $T = 25^\circ\text{C}$ . **b)** Titration of a 20 mM G-C18:1 solution with 50 mM  $\text{CaCl}_2$  solution. Fit (red line) is performed with a multiple site model; **c)** Titration of a 5 mM G-C18:1 solution with 32 mM  $\text{AgNO}_3$  solution. Fit (red line) is performed with an independent model. Raw ITC data are given in Figure S 3.

ITC is corroborated by both mechanistic and structural data. Cation-resolved *in situ* SAXS performed on  $\{\text{Ca}^{2+}\}\text{G-C18:1}$  shows the existence of two interaction steps when the calcium content is increased with respect to G-C18:1.<sup>33</sup> Two critical  $[\text{Ca}^{2+}]:[\text{G-C18:1}]$  molar ratios were also identified: the value of 0.25, in very good agreement with the minimum of the bell-shaped ITC curve in Figure 5b, triggers the micelle-to-fiber transition, while the value of 0.7 triggers



the intra-fiber crystallization. Interestingly, *in situ* SAXS could not be performed on {Ag<sup>+</sup>}G-C18:1, as its reactivity was too fast to be compatible with the experimental setup. This observation is also in line with the single reaction step found by ITC.

ITC and SAXS data are also corroborated by <sup>13</sup>C solid-state cross polarization (CP) magic angle spinning (MAS) nuclear magnetic resonance (NMR) recorded on freeze-dried G-C18:1 micelles and {Ca<sup>2+</sup>}G-C18:1 and {Ag<sup>+</sup>}G-C18:1 gels (fresh gels cannot be studied due to sample centrifugation during MAS, here having a frequency of 10 kHz). Figure 6 highlights the 160-200 ppm (C=O) and 60-110 ppm (glucose) regions. All signal related to glucose (1', 6' and the group 2', 5', 3', 4') are equally broad and set at the same chemical shift for all samples, indicating that glucose is not relevantly involved in the structural differences between the G-C18:1 samples. On the other hand, the C=O signal is broad for the micellar samples (δ= 182 ppm), sharp but split in two signals for {Ca<sup>2+</sup>}G-C18:1 (δ<sub>1</sub>= 184 ppm, δ<sub>2</sub>= 179 ppm) and sharp for {Ag<sup>+</sup>}G-C18:1 (δ= 179.5 ppm). If the broad signal in the micellar sample indicates a dispersion in the C=O configurations, the sharp peaks for {Ag<sup>+</sup>}G-C18:1 and {Ca<sup>2+</sup>}G-C18:1 are the proof of magnetically-equivalent chemical environments, as expected for crystalline samples. Their chemical shifts variations between the micellar and fiber forms provide a proof that interactions occur between the C=O and the metal ions. The splitting observed for the C=O signal in {Ca<sup>2+</sup>}G-C18:1 is a confirmation that C=O has two chemically-inequivalent positions, as supposed on the basis of ITC (Figure 5b) and SAXS<sup>33</sup> arguments.

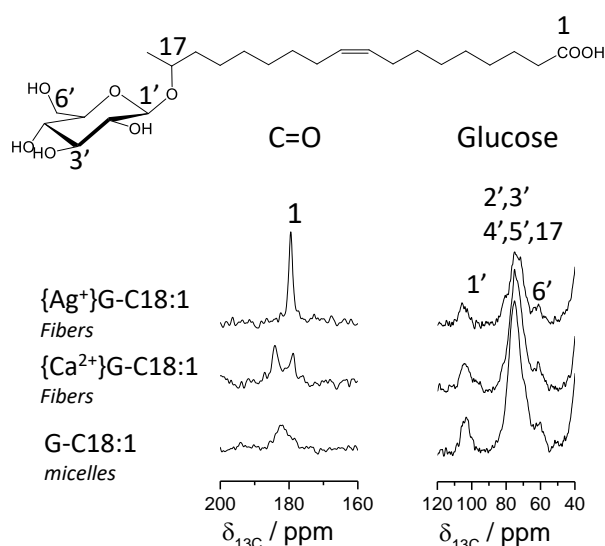


**Figure 6 - Solid-state <sup>13</sup>C CP MAS NMR spectra recorded on freeze-dried samples prepared from G-C18:1 micellar solution ( $t_c = 1$  ms), {Ca<sup>2+</sup>}G-C18:1 gel ( $t_c = 3$  ms), {Ag<sup>+</sup>}G-C18:1 gel ( $t_c = 1$  ms).  $t_c$  stands for the contact time related to the magnetization transfer from <sup>1</sup>H to <sup>13</sup>C during cross polarization.**

### *Understanding the $\beta$ -sheet-like raft structure*

Although the present state of the art does not yet provide a full understanding and prediction about the effects of cations on the molecular structure and collective organization of amphiphiles in water, the abundant literature presenting the effects of cations on the self-assembly of amphiphiles<sup>41,55,98</sup> (more extensive literature survey given in Ref. <sup>31</sup>) could help understanding our data. Calcium and silver G-C18:1 hydrogels have similar structures, equivalent gel strength,<sup>32</sup> resistance to temperature<sup>32</sup> and mechanism of formation.<sup>33</sup> These data could be explained by the fact that the COO<sup>-</sup> group of G-C18:1 is a good ligand for Ca<sup>2+</sup> and Ag<sup>+</sup>,<sup>99–101</sup> which exist as free ions at pH below about 10.<sup>102</sup> Figure 7 shows the overview of the fibrillation process and  $\beta$ -sheet-like raft formation in {Ag<sup>+</sup>}G-C18:1 and {Ca<sup>2+</sup>}G-C18:1 systems.

*Fibers' formation.* ITC, cation-resolved *in situ* SAXS<sup>33</sup> and <sup>13</sup>C CP MAS NMR all confirm the critical role of Ag<sup>+</sup> and Ca<sup>2+</sup> in promoting the micelle-to-fiber transition, compared to the negative control, Na<sup>+</sup>.

In the case of silver, the fiber's lateral width of about 5 nm is compatible with two aligned G-C18:1 molecules. The most obvious arrangement is depicted in Figure 7b, whereas the fiber's thickness is supposed to be molecular. Silver is coordinated by the carboxylate groups,<sup>99,102–104</sup> as found for other fatty acid silver complexes.<sup>82–84</sup> Such dimeric building unit within the fibers, of which the core is rich in cations and the external sides in glucose, is actually similar to what has been reported for silver stearate<sup>84</sup> or bile salts.<sup>69</sup> The coordination reaction is demonstrated by the more shielded <sup>13</sup>C chemical shift of the sharp C=O peak associated to the silver fibers and compared to the micelles. The reaction is highly exothermic and extremely rapid, as shown by ITC, but also by the impossibility to run silver-resolved *in situ* SAXS experiments on this system.<sup>33</sup> The same lamellar order is in fact observed even under dilute conditions (Figure S 1). Overall, the reactivity of silver towards carboxylate groups does not allow a continuous micelle-to-fiber transition, but it probably induces a diffusion of G-C18:1 molecules from the micelles towards the metal ions, where micelles then become a reservoir of matter, rather than nucleation sites. A similar mechanism was proposed for the pH-triggered fibrillation of C18:0 sophorolipids.<sup>35</sup>

In the case of calcium, the mechanism and the fiber's structure is more complex. At a first stage, according to ITC and calcium-resolved *in situ* SAXS,<sup>33</sup> possible combination of sodium-calcium exchange and hydrophobic effect drive the fibers' formation, possibly through the formation of flip-flopped G-C18:1 dimers. These are not unexpected, as vesicle membranes composed of G-C18:1 are interdigitated.<sup>34,35</sup> Flip-flopped dimers drive the morphological

evolution at least until  $[\text{Ca}^{2+}]/[\text{G-C18:1}]$  in the order of 0.5-0.6, that is until complete charge matching, according to *in situ* SAXS data.<sup>33</sup> A second step in the self-assembly of  $\{\text{Ca}^{2+}\}\text{G-C18:1}$  occurs above a molar ratio of 0.6. The exothermic reaction probed by ITC must be understood in relationship to a ligand-ion binding,<sup>92,96</sup> probably driven by the proximity between  $\text{COO}^-$  and  $\text{Ca}^{2+}$  inside, but also, across the fibers, in analogy to the “egg-box” structures.<sup>77,90</sup> This is confirmed by the crystallization phenomenon above a ratio of 0.6 (but probably occurring at a lower ratio) shown by the *in situ* SAXS data.<sup>33</sup> It must be believed that the strong bidentate binding of carboxylate to calcium combined to the specific coordination geometry of the latter<sup>100</sup> and packing constraints of G-C18:1 drive the fibers’ crystallization process. Crystallization is certainly driven by a massive coordinating effect of calcium, as expected<sup>100,101</sup> and actually found in many other systems, including alginate.<sup>90</sup> The interaction between  $\text{COO}^-$  and  $\text{Ca}^{2+}$  is obvious when looking at the  $^{13}\text{C}$  CP MAS NMR data, and in particular at the difference in the  $^{13}\text{C}$  chemical shift of the C=O group between the micellar and fibrillar environment.

The crystal structure is certainly associated to the fiber itself, although calcium-mediated coordination between fibers are also expected, as discussed further down. Nonetheless, this behavior seems to be peculiar only for G-C18:1, as no morphological changes are experienced by similar glycolipids (C18:1 sophorolipids, rhamnolipids) in solution when exposed to a calcium source.<sup>105,106</sup> Differently than silver,  $\{\text{Ca}^{2+}\}\text{G-C18:1}$  materials are obtained through a continuous morphological evolution from micelles to fibers,<sup>33</sup> as also observed during the fibrillation of C16:0 sophorolipids.<sup>107</sup>

The complexity of the diffraction pattern in the SAXS profiles of  $\{\text{Ca}^{2+}\}\text{G-C18:1}$  does not unfortunately provide a clear-cut answer about its crystal structure, but one can state that a 2D oblique lattice must be employed to account for the diffraction pattern (Figure S 2). We do suppose that the flip-flopped dimers constituting the oblique lattice are in the plane of the fiber, as shown in Figure 7a and as found for other cation-mediated fibrillar systems prepared under dilute conditions.<sup>108,109</sup> We do exclude the possibility of a ribbon phase, in which the oblique lattice would be orthogonal to the fiber’s longitudinal axis (Figure S 2b), because this phase is generally observed for highly concentrated lyotropic liquid crystals,<sup>110,111</sup> while the G-C18:1 concentrations studied here are below 5 wt%. The approximate cross-section of the fibers is 10 nm, meaning that at least four G-C18:1 molecules are packed. All in all, calcium seems to play a double role, charge screening at low ion-to-lipid ratio, and coordinating ion at high ratio.

Some considerations about the role of the glucose headgroup. The important role of glucose is confirmed by the absence of morphological evolution when sister molecules like C18:1

sophorolipids (two glucose units) or rhamnolipids (a rhamnose unit) are studied in the presence of mono and divalent cations.<sup>105,106</sup> However, a specific structural, or driving, role of glucose is most likely excluded on the basis of  $^{13}\text{C}$  CP MAS NMR experiments, which show an invariant signal within the micellar phase and fiber structures. Even if glucose plays a side role, this is still important.

In the absence of glucose, one would expect the precipitation of a crystal, as found for silver stearate.<sup>84</sup> Its hydrophilic nature combined to the bolaform structure of G-C18:1 then certainly contribute to the colloidal stability of the fibers in water. On the other side, its bulkiness could also have an impact on the fibers' twist and side-by-side packing. The circular dichroism (CD) signal of  $\{\text{Ca}^{2+}\}\text{G-C18:1}$  demonstrates an optical activity for this material, compared to  $\{\text{Ag}^+\}\text{G-C18:1}$  (Figure S 4) or to a micellar solution of G-C18:1 (flat line, no optical activity, not shown), making it structurally similar to sophorolipid ribbons.<sup>62</sup> The difference between the CD signal of  $\{\text{Ca}^{2+}\}\text{G-C18:1}$  and the typical CD spectrum of  $\beta$ -sheets in proteins<sup>112</sup> confirms that one can only speak of analogues of  $\beta$ -sheets ( *$\beta$ -sheet-like rafts*) for  $\{\text{Ca}^{2+}\}\text{G-C18:1}$ .

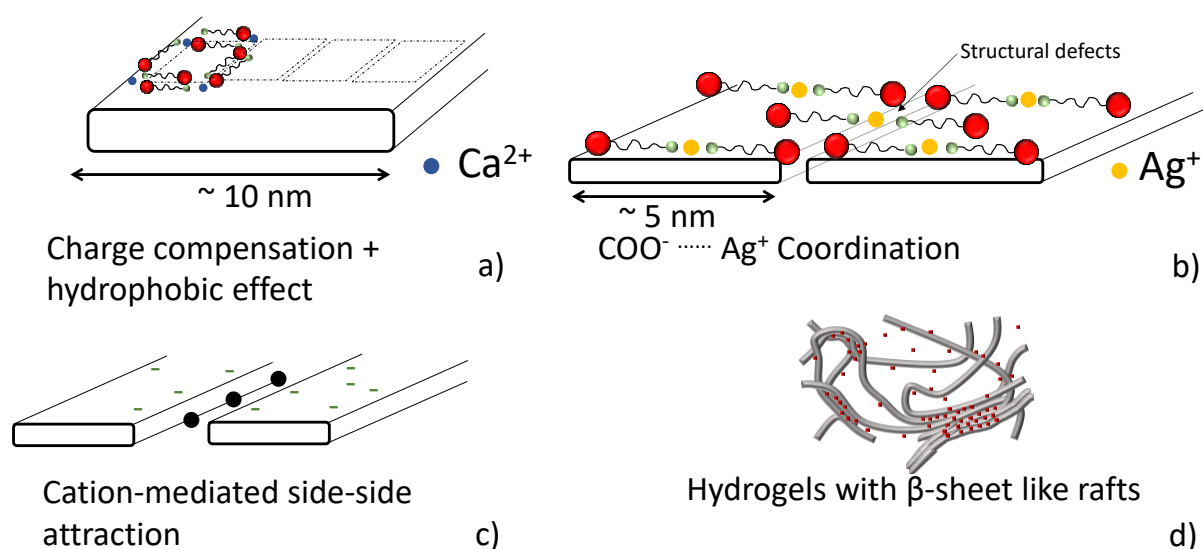


**Figure 7 - Scheme of the possible hierarchical self-assembled structures found in a)  $\{\text{Ca}^{2+}\}\text{G-C18:1}$  and b)  $\{\text{Ag}^+\}\text{G-C18:1}$  gels. c) Illustration of the possible side-by-side, cation-mediated, interaction between  $\{\text{Ca}^{2+}\}\text{G-C18:1}$  and  $\{\text{Ag}^+\}\text{G-C18:1}$  fibers. d) “Nano fishnet” model structure of  $\{\text{Ca}^{2+}\}\text{G-C18:1}$  and b)  $\{\text{Ag}^+\}\text{G-C18:1}$  gels.**

*Lateral association into  $\beta$ -sheet-like rafts.* The difference between hexagonal bundles and lamellar rafts lies in the anisotropy of the driving forces around each fiber. Previously reported cylindrical fibers, tubules or even flat fibers are generally described having an isotropic distribution of charges around the cross section, driving the system to the hexagonal packing,

the most energetically favorable structure for packed cylinders.<sup>25,26</sup> In the case of side-by-side interactions leading to multimers and raft, one must invoke the presence of an orientational force located at the external edge of the fibers, such as bridge-like cross-linking events driven by the cation, as found for alginate.<sup>90</sup> In the case of proteins, the driving force to obtain  $\beta$ -sheets could be explained by possible multipolar moments, as intended by Van Workum et al.<sup>113</sup> However, the amphiphilic nature of G-C18:1, the absence of amino acids in its molecular structure and, above all, the set of ITC and  $^{13}\text{C}$  CP MAS NMR experiments strongly supports specific metal-ligand interaction as being the main driving force.<sup>30</sup>

In the case of silver, the linear dimeric association of G-C18:1 results in the outward orientation of glucose at the side edges of the fibers. Directional side-by-side fiber attraction (Figure 7c) could then be driven by a number of phenomena, such as sugar-sugar interactions (hydrogen bonding, Van der Waals attraction) counterbalanced by repulsive short-range hydration forces<sup>60,114</sup> or cation-mediated interactions. In the latter, one could certainly suppose cation adsorption onto the neutral glucose layer, as recently reported for glycolipid membranes,<sup>115</sup> but silver-carboxylate coordination across adjacent fibers is the most plausible hypothesis. In this regard, one must suppose the existence of structural flip-flop defects in the silver-G-C18:1 packing within the fiber plane, as proposed in Figure 7b. Flip-flop, which maximizes packing and minimizes repulsive steric interactions among sugar headgroups, was previously proposed in the case of interdigitated membranes composed of G-C18:1 and G-C18:0.<sup>34,35,54</sup> This hypothesis could also well agree with the narrower size of  $\beta$ -sheet-like rafts observed in  $\{\text{Ag}^+\}\text{G-C18:1}$  compared to the calcium system: few and unevenly distributed flip-flop defects along the fiber's axis could drive the formation of dimers or trimers (Figure 3b,e,f), instead of large rafts (Figure 3a,c,d).

The cation-mediated mechanism of lateral attraction among fibers, resulting in the formation of wide  $\beta$ -sheet-like rafts, appears to be very important for  $\{\text{Ca}^{2+}\}\text{G-C18:1}$  hydrogels (Figure 7c). The existence of an inter-fibrillar complexation site is a hypothesis, which seems to be corroborated by the splitting of the  $\text{C}=\text{O}$  peak in the  $^{13}\text{C}$  CP MAS NMR spectrum of  $\{\text{Ca}^{2+}\}\text{G-C18:1}$ .

*Hydrogel formation and stability.* When lamellar rafts form, face-to-face dispersive forces should drive attraction between rafts and induce precipitation of lamellar crystals.<sup>27,81</sup> This does not seem to occur for  $\{\text{Ca}^{2+}\}\text{G-C18:1}$  and  $\{\text{Ag}^+\}\text{G-C18:1}$  hydrogels. One must then suppose the presence of repulsive forces acting between the fibers' faces. Hydration forces<sup>114</sup> are short-ranged ( $< 3$  nm) and they are therefore excluded. Possible long-range repulsive forces could be

attributed to electrostatic or steric interactions. Electrostatic forces could draw their origin from carboxylic groups oriented orthogonally to the fiber's plane. However, this hypothesis is highly unlikely for the number of structural considerations commented above. Condensation of ions, a well-known phenomenon in amphiphiles,<sup>116–118</sup> is a plausible mechanism considering the fact that the colloidal stability of the fibers and gel formation are not perturbed by excess ions ( $[M^{z+}]/[G-C18:1] > 1$ ).<sup>32</sup> However, studying this mechanism would require a dedicated effort out of the scope of this work.

Helfrich undulations are another important long-range steric repulsive force found in lipid bilayer membranes and explaining the extreme swelling of lamellar phases.<sup>119</sup> Cryo-TEM (Figure 3) shows that the fibers, individual or associated, are flexible at scales above 100 nm. These undulations, with periods in the order of 200-500 nm, are compatible with the typical undulation wavelengths reported for swollen lamellar phases. Interestingly, neutron spin-echo experiments, commonly used to measure the stiffness of soft membranes,<sup>120</sup> run on the  $\{Ca^{2+}\}G-C18:1$  fiber hydrogels (Figure 5a) show a slower decay of the spin echo intensity than in vesicles, with a  $\frac{\Gamma_{ZG}}{q^3}$  (Eq. S2) about two orders of magnitude lower ( $\sim 5 \cdot 10^{-2} \text{ nm}^3/\text{ns}$  for vesicles against  $\sim 1 \cdot 10^{-3} \text{ nm}^3/\text{ns}$  for fibers). Since  $\frac{\Gamma_{ZG}}{q^3}$  is inversely proportion to the bending rigidity (Eq. S3), NSE data confirms that fibers are more rigid than vesicles in the meso scale (4-8 nm), confirming the strong effect of  $Ca^{2+}$  on the collective dynamics of G-C18:1.

If the hypothesis of undulation forces is not unreasonable, the rigidity of fibrillar  $\{Ca^{2+}\}G-C18:1$  hydrogels must probably be compared to stiff lamellar  $L_\beta$  phases<sup>121</sup> than to swollen lamellar phases.<sup>122</sup> The different order between  $\{Ca^{2+}\}G-C18:1$  fibers (crystalline) and G-C18:1 vesicle (liquid crystalline) could certainly explain the discrepancy and it should be said that we are not aware of bending rigidity studies on crystalline fibers using neutron spin echo so as to compare our data with. Further work could dissipate the present doubts.

Both  $Ca^{2+}$  and  $Ag^+$  play an important structural role in the fiber's formation and stability. This can be easily tested by adding a competitive anion to the  $\{Ca^{2+}\}G-C18:1$  and  $\{Ag^+\}G-C18:1$  gel solutions. Figure S 5 shows that EDTA, a well-known  $Ca^{2+}$  complexing agent, or chloride anions, precipitating silver, destabilize  $\{Ca^{2+}\}G-C18:1$  and  $\{Ag^+\}G-C18:1$  hydrogels, respectively. Interestingly, the process is reversible, as a novel source of calcium, or silver, ions to the destabilized sols induce gelation again.

## Conclusions

SAFiN from low molecular weight compounds commonly form hydrogels under dilute conditions, generally in the order of 1 wt% or less. Whatever the stimulus (temperature, pH, ionic strength) that drives fibrillation and consequent hydrogel formation, the structure of the gel is generally very similar across samples of different origin. SAFiN hydrogels are formed by an entangled network of infinitely long fibers. The typical X-ray or neutron scattering profiles display the form, and sometimes structure, a factor of individual fibers. In some specific cases, fibers form columnar structures (bundles) with a hexagonal order, driven by repulsive electrostatic interactions.

In this work, we report the “nano-fishnet” structure of self-assembled fibrillar hydrogels prepared from an amphiphile. Metal-ligand complexation between  $\text{Ca}^{2+}$ , or  $\text{Ag}^+$ , ions and the  $\text{COO}^-$  group of a natural glycolipid, G-C18:1, drives gelation. The “nano-fishnet” structure, which combines entanglement and  $\beta$ -sheet domains, is not known for amphiphile SAFiN hydrogels but rather reported for more complex aminoacid-based systems, like natural actin and silk proteins. G-C18:1 does not contain aminoacids and it does form  $\beta$ -sheets, as verified by circular dichroism. However, the combination of cryo-TEM and SAXS experiments shows a structural analogy between G-C18:1 and silk fibroin hydrogels, thus motivating the description of the lateral association of G-C18:1 fibers as  $\beta$ -sheet-like rafts.

G-C18:1 is a novel bolaform glucolipid containing a free-standing  $\text{COOH}$  group and belonging to the broad family of biological amphiphiles (biosurfactants). In its micellar phase at pH above neutrality, the addition of a  $\text{Ca}^{2+}$  or  $\text{Ag}^+$  solution drives a micelle-to-fiber phase transition, not expected for specific compound. Fibers have an approximate cross-section of 10 and 5 nm, respectively for  $\{\text{Ca}^{2+}\}$ G-C18:1 and  $\{\text{Ag}^+\}$ G-C18:1 systems. Above about 0.5 wt%, the addition of the ion solution also drives the formation of a hydrogel, of which the strength is maximized at a stoichiometric negative/positive charge ratio between the  $\text{COO}^-$  group of the glucolipid and the cation. The gel strength ( $G'$ ) increases with glucolipid concentration according to a power law dependency in the order of 2.3-2.6. The strength of the hydrogels is one order of magnitude higher for  $\{\text{Ag}^+\}$ G-C18:1 with respect to  $\{\text{Ca}^{2+}\}$ G-C18:1 and so is the stability against shearing and temperature, shown elsewhere.<sup>32</sup>

$\{\text{Ag}^+\}$ G-C18:1 hydrogels display a long-range lamellar order of the fibers, systematically observed at rest, independently of shear, heating or combination of both.<sup>32</sup> Such order is observed both by cryo-TEM, showing how individual fibers spontaneously assemble into lamellar multimers, and, above all, SAXS. Similar results are also observed for  $\{\text{Ca}^{2+}\}$ G-C18:1 hydrogels, although the lamellar structure factor is partially or totally lost when hydrogels are sheared.

The structural SAXS and cryo-TEM data prone for a “nano-fishenet” structure of both  $\{\text{Ca}^{2+}\}$ G-C18:1 and  $\{\text{Ag}^+\}$ G-C18:1 hydrogels up to at least 5 wt% of glucolipid in solution. The strong stability towards shear and temperature can probably be explained by such  $\beta$ -sheet-like raft structure.

The main hypothesis explaining the existence of  $\beta$ -sheet-like rafts concerns the anisotropic distribution of negative charges in the fibers, most likely located on the fibers alongside. The counterions would then act as “glue” across adjacent fibers through charge-screening or coordination interactions. Isothermal titration calorimetry and  $^{13}\text{C}$  CP MAR NMR corroborate this hypothesis. ITC shows a strong exothermic signal, typical for specific interactions, when cations are added to the solution. NMR shows variation in chemical shift and narrowing of the C=O peak when G-C18:1 changes from the micellar to the fibrillar environment. ITC, combined with complementary ion-resolved *in situ* SAXS experiments presented elsewhere,<sup>33</sup> also shows important differences between the calcium and silver systems. In  $\{\text{Ca}^{2+}\}$ G-C18:1, negatively charged G-C18:1 micelles undergo a continuous micelle-to-fiber morphological transition with two well-identified steps: low calcium content ( $< 0.3$  molar ratio) favors the micelle-to-fiber transition, while high calcium concentration ( $> 0.3$  molar ratio) favors fiber crystallization. In  $\{\text{Ag}^+\}$ G-C18:1, negatively-charged micelles serve as a reservoir of matter for G-C18:1 molecules: silver ions immediately react with G-C18:1 to form dimers, which promptly associate into fibers.

## Acknowledgements

We thank Dr. S. Roelants at Gent University and Bio Base Europe Pilot Plant, Gent, Belgium for dealing with and shipping the G-C18:1 glycolipid. Authors kindly acknowledge the French ANR, Project N° SELFAMPHI - 19-CE43-0012-01. Soleil synchrotron is acknowledged for financial support during the beamtime associated to the proposal number N°20201747. ESRF synchrotron is acknowledged for financial support during the beamtime associated to the proposal numbers N°MX 2311. Laurent Michot (Sorbonne Université, Paris, France) is kindly acknowledged for sharing the beamtime (Proposal N°: BAG 20201118) on the SWING beamline at Soleil synchrotron, Saint-Aubin, France. Marianne Impérator-Clerc (Université Paris-Saclay, France) is acknowledged for helpful discussions. This work has been sponsored by the Ile-de-France Region in the framework of the DIM Respire, the Ile-de-France network of Excellence in Porous Solids. Raw data from NSE measurements is available under [dx.doi.org/10.5291/ILL-DATA.9-13-915](https://dx.doi.org/10.5291/ILL-DATA.9-13-915).



## References

- (1) Raghavan, S. R.; Douglas, J. F. The Conundrum of Gel Formation by Molecular Nanofibers, Wormlike Micelles, and Filamentous Proteins: Gelation without Cross-Links? *Soft Matter* **2012**, *8*, 8539.
- (2) Ahsan, A.; Tian, W. X.; Farooq, M. A.; Khan, D. H. An Overview of Hydrogels and Their Role in Transdermal Drug Delivery. *Int. J. Polym. Mater. Polym. Biomater.* **2020**, *0*, 1–11.
- (3) Wichterle, O.; Lim, D. Hydrophilic Gels for Biological Use. *Nature* **1960**, *185*, 117–118.
- (4) Van Vlierberghe, S.; Dubruel, P.; Schacht, E. Biopolymer-Based Hydrogels as Scaffolds for Tissue Engineering Applications: A Review. *Biomacromolecules* **2011**, *12*, 1387–1408.
- (5) Tam, A. Y. Y.; Yam, V. W. W. Recent Advances in Metallogels. *Chem. Soc. Rev.* **2013**, *42*, 1540–1567.
- (6) Piepenbrock, M. M.; Lloyd, G. O.; Clarke, N.; Steed, J. W. Metal- and Anion-Binding Supramolecular Gels. **2010**, 1960–2004.
- (7) Draper, E. R.; Su, H.; Brasnett, C.; Poole, R. J.; Rogers, S.; Cui, H.; Seddon, A.; Adams, D. J. Opening a Can of Worm(-like Micelle)s: The Effect of Temperature of Solutions of Functionalized Dipeptides. *Angew. Chemie* **2017**, *129*, 10603–10606.
- (8) Adams, D. J.; Butler, M. F.; Frith, W. J.; Kirkland, M.; Mullen, L.; Sanderson, P. A New Method for Maintaining Homogeneity during Liquid-Hydrogel Transitions Using Low Molecular Weight Hydrogelators. *Soft Matter* **2009**, *5*, 1856–1862.
- (9) Carretti, E.; Mazzini, V.; Fratini, E.; Ambrosi, M.; Dei, L.; Baglioni, P.; Lo Nostro, P. Structure and Rheology of Gel Nanostructures from a Vitamin C-Based Surfactant. *Phys. Chem. Chem. Phys.* **2016**, *18*, 8865–8873.
- (10) Draper, E. R.; Adams, D. J. Low-Molecular-Weight Gels: The State of the Art. *Chem* **2017**, *3*, 390–410.
- (11) Yu, G.; Yan, X.; Han, C.; Huang, F. Characterization of Supramolecular Gels. *Chem. Soc. Rev.* **2013**, *42*, 6697–6722.
- (12) Rathore, O.; Sogah, D. Y. Nanostructure Formation through  $\beta$ -Sheet Self-Assembly in Silk-Based Materials. *Macromolecules* **2001**, *34*, 1477–1486.
- (13) Fink, T. D.; Zha, R. H. Silk and Silk-Like Supramolecular Materials. *Macromol. Rapid Commun.* **2018**, *39*, 1–17.
- (14) Kim, U. J.; Park, J.; Li, C.; Jin, H. J.; Valluzzi, R.; Kaplan, D. L. Structure and Properties

- of Silk Hydrogels. *Biomacromolecules* **2004**, *5*, 786–792.
- (15) Liu, R.; Deng, Q.; Yang, Z.; Yang, D.; Han, M. Y.; Liu, X. Y. “Nano-Fishnet” Structure Making Silk Fibers Tougher. *Adv. Funct. Mater.* **2016**, *26*, 5534–5541.
  - (16) Gardel, M. L.; Shin, J. H.; MacKintosh, F. C.; Mahadevan, L.; Matsudaira, P.; Weitz, D. A. Elastic Behavior of Cross-Linked and Bundled Actin Networks. *Science (80-. )*. **2004**, *304*, 1301–1305.
  - (17) Pelletier, O.; Pokidysheva, E.; Hirst, L. S.; Boussein, N.; Li, Y.; Safinya, C. R. Structure of Actin Cross-Linked with [Formula Presented]-Actinin: A Network of Bundles. *Phys. Rev. Lett.* **2003**, *91*, 3–6.
  - (18) Wong, G. C. L.; Lin, A.; Tang, J. X.; Li, Y.; Janmey, P. A.; Safinya, C. R. Lamellar Phase of Stacked Two-Dimensional Rafts of Actin Filaments. *Phys. Rev. Lett.* **2003**, *91*, 1–4.
  - (19) Ochi, A.; Hossain, K. S.; Ooyama, E.; Magoshi, J.; Nemoto, N. Dynamic Light Scattering of Native Silk Fibroin Solution Extracted from Different Parts of the Middle Division of the Silk Gland of the Bombyx Mori Silkworm. *Biomacromolecules* **2003**, *4*, 350–359.
  - (20) Calabrese, V.; Muñoz-García, J. C.; Schmitt, J.; da Silva, M. A.; Scott, J. L.; Angulo, J.; Khimyak, Y. Z.; Edler, K. J. Understanding Heat Driven Gelation of Anionic Cellulose Nanofibrils: Combining Saturation Transfer Difference (STD) NMR, Small Angle X-Ray Scattering (SAXS) and Rheology. *J. Colloid Interface Sci.* **2019**, *535*, 205–213.
  - (21) Okesola, B. O.; Wu, Y.; Derkus, B.; Gani, S.; Wu, D.; Knani, D.; Smith, D. K.; Adams, D. J.; Mata, A. Supramolecular Self-Assembly to Control Structural and Biological Properties of Multicomponent Hydrogels. *Chem. Mater.* **2019**, *31*, 7883–7897.
  - (22) Yu, Z.; Tantanitti, F.; Palmer, L. C.; Stupp, S. I. Asymmetric Peptide Nanoribbons. *Nano Lett.* **2016**, *16*, 6967–6974.
  - (23) Draper, E. R.; Dietrich, B.; McAulay, K.; Brasnett, C.; Abdizadeh, H.; Patmanidis, I.; Marrink, S. J.; Su, H.; Cui, H.; Schweins, R.; et al. Using Small-Angle Scattering and Contrast Matching to Understand Molecular Packing in Low Molecular Weight Gels. *Matter* **2020**, *2*, 764–778.
  - (24) McAulay, K.; Wang, H.; Fuentes-Caparrós, A. M.; Thomson, L.; Khunti, N.; Cowieson, N.; Cui, H.; Seddon, A.; Adams, D. J. Isotopic Control over Self-Assembly in Supramolecular Gels. *Langmuir* **2020**, *36*, 8626–8631.
  - (25) Terech, P.; Maitra, U. Structural and Rheological Properties of Aqueous Viscoelastic Solutions and Gels of Tripodal Chalamide-Based Self-Assembled Supramolecules. *J.*

- Phys. Chem. B* **2008**, *112*, 13483–13492.
- (26) Cui, H.; Pashuck, E. T.; Velichko, Y. S.; Weigand, S. J.; Cheetham, A. G.; Newcomb, C. J.; Stupp, S. I. Spontaneous and X-Ray–Triggered Crystallization at Long Range in Self-Assembling Filament Networks. *Science* (80-. ). **2010**, *327*, 555–560.
  - (27) Weingarten, A. S.; Kazantsev, R. V.; Palmer, L. C.; McClendon, M.; Koltonow, A. R.; Samuel, A. P. S.; Kieba, D. J.; Wasielewski, M. R.; Stupp, S. I. Self-Assembling Hydrogel Scaffolds for Photocatalytic Hydrogen Production. *Nat. Chem.* **2014**, *6*, 964–970.
  - (28) Paineau, E.; Rouzière, S.; Monet, G.; Diogo, C. C.; Morfin, I.; Launois, P. Role of Initial Precursors on the Liquid-Crystalline Phase Behavior of Synthetic Aluminogermanate Imogolite Nanotubes. *J. Colloid Interface Sci.* **2020**, *580*, 275–285.
  - (29) Saerens, K. M. J.; Zhang, J.; Saey, L.; Van Bogaert, I. N. A.; Soetaert, W. Cloning and Functional Characterization of the UDP-Glucosyltransferase UgtB1 Involved in Sophorolipid Production by *Candida Bombicola* and Creation of a Glucolipid-Producing Yeast Strain. *Yeast* **2011**, *28*, 279–292.
  - (30) Baccile, N.; Poirier, A.; Seyrig, C.; Griel, P. Le; Perez, J.; Hermida-Merino, D.; Pernot, P.; Roelants, S.; Soetaert, W. Chameleonic Amphiphile: The Unique Multiple Self-Assembly Properties of a Natural Glycolipid in Excess of Water. *J. Colloid Interface Sci.* **2023**, *630*, 404–415.
  - (31) Poirier, A.; Griel, P. Le; Perez, J.; Hermida-Merino, D.; Pernot, P.; Baccile, N. Metallogels from Glycolipid Biosurfactant. *ACS Sustain. Chem. Eng.* **2022**, Just Accepted, DOI: 10.1021/acssuschemeng.2c01860.
  - (32) Poirier, A.; Bizien, T.; Zinn, T.; Pernot, P.; Baccile, N. Shear Recovery and Temperature Stability of Ca<sup>2+</sup> and Ag<sup>+</sup> Glycolipid Fibrillar Metallogels with Unusual  $\beta$ -Sheet-like Domains. *Soft Matter* **2022**, Just Accepted, DOI: 10.1039/d2sm00374k.
  - (33) Poirier, A.; Griel, P. Le; Perez, J.; Baccile, N. Cation-Induced Fibrillation of Microbial Glycolipid Biosurfactant Probed by Ion-Resolved In Situ SAXS. *J. Phys. Chem. B* **2022**, Just Accepted, DOI: 10.1021/acs.jpcc.2c03739.
  - (34) Baccile, N.; Selmane, M.; Le Griel, P.; Prévost, S.; Perez, J.; Stevens, C. V.; Delbeke, E.; Zibek, S.; Guenther, M.; Soetaert, W.; et al. PH-Driven Self-Assembly of Acidic Microbial Glycolipids. *Langmuir* **2016**, *32*, 6343–6359.
  - (35) Baccile, N.; Cuvier, A.-S.; Prévost, S.; Stevens, C. V.; Delbeke, E.; Berton, J.; Soetaert, W.; Van Bogaert, I. N. A.; Roelants, S. Self-Assembly Mechanism of PH-Responsive Glycolipids: Micelles, Fibers, Vesicles, and Bilayers. *Langmuir* **2016**, *32*, 10881–10894.

- (36) Angelescu, D.; Caldararu, H.; Khan, A. Some Observations on the Effect of the Trivalent Counterion  $Al^{3+}$  to the Self-Assembly of Sodium Dodecyl Sulphate in Water. *Colloids Surfaces A Physicochem. Eng. Asp.* **2004**, *245*, 49–60.
- (37) Vasilescu, M.; Angelescu, D.; Caldararu, H.; Almgren, M.; Khan, A. Fluorescence Study on the Size and Shape of Sodium Dodecyl Sulphate-Aluminium Salt Micelles. *Colloids Surfaces A Physicochem. Eng. Asp.* **2004**, *235*, 57–64.
- (38) Srinivasan, V.; Blankschtein, D. Effect of Counterion Binding on Micellar Solution Behavior: 2. Prediction of Micellar Solution Properties of Ionic Surfactant-Electrolyte Systems. *Langmuir* **2003**, *19*, 9946–9961.
- (39) Qiao, Y.; Lin, Y.; Wang, Y.; Li, Z.; Huang, J. Metal-Driven Viscoelastic Wormlike Micelle in Anionic/Zwitterionic Surfactant Systems and Template-Directed Synthesis of Dendritic Silver Nanostructures. *Langmuir* **2011**, *27*, 1718–1723.
- (40) Guo, J.; Li, Y.; Zhang, Y.; Ren, J.; Yu, X.; Cao, X. Switchable Supramolecular Configurations of  $Al^{3+}$ /LysTPY Coordination Polymers in a Hydrogel Network Controlled by Ultrasound and Heat. *ACS Appl. Mater. Interfaces* **2021**, *13*, 40079–40087.
- (41) Chen, L.; McDonald, T. O.; Adams, D. J. Salt-Induced Hydrogels from Functionalised-Dipeptides. *RSC Adv.* **2013**, *3*, 8714–8720.
- (42) Zhou, X. R.; Ge, R.; Luo, S. Z. Self-Assembly of PH and Calcium Dual-Responsive Peptide-Amphiphilic Hydrogel. *J. Pept. Sci.* **2013**, *19*, 737–744.
- (43) Xie, Y.; Zhao, J.; Huang, R.; Qi, W.; Wang, Y.; Su, R.; He, Z. Calcium-Ion-Triggered Co-Assembly of Peptide and Polysaccharide into a Hybrid Hydrogel for Drug Delivery. *Nanoscale Res. Lett.* **2016**, *11*, 184.
- (44) Greenfield, M. A.; Hoffman, J. R.; De La Cruz, M. O.; Stupp, S. I. Tunable Mechanics of Peptide Nanofiber Gels. *Langmuir* **2010**, *26*, 3641–3647.
- (45) Shi, J.; Gao, Y.; Zhang, Y.; Pan, Y.; Xu, B. Calcium Ions to Cross-Link Supramolecular Nanofibers to Tune the Elasticity of Hydrogels over Orders of Magnitude. *Langmuir* **2011**, *27*, 14425–14431.
- (46) Seyrig, C.; Kignelman, G.; Thielemans, W.; Griel, P. Le; Cowieson, N.; Perez, J.; Baccile, N. Stimuli-Induced Non-Equilibrium Phase Transitions in Polyelectrolyte-Surfactant Complex Coacervates. *Langmuir* **2020**, *36*, 8839–8857.
- (47) Renterghem, L. Van; Guzzetta, F.; Le Griel, P.; Selmane, M.; Messaoud, G. Ben; Teng, T. T. S.; Lim, S.; Soetaert, W.; Roelants, S.; Julián-López, B.; et al. Easy Formation of Functional Liposomes in Water Using a PH-Responsive Microbial Glycolipid:

- Encapsulation of Magnetic and Upconverting Nanoparticles. *ChemNanoMat* **2019**, *5*, 1188–1201.
- (48) Song, A.; Hao, J. Self-Assembly of Metal-Ligand Coordinated Charged Vesicles. *Curr. Opin. Colloid Interface Sci.* **2009**, *14*, 94–102.
- (49) De Gennes, P.-G. Dynamics of Entangled Polymer Solutions. I. The Rouse Model. *Macromolecules* **1976**, *9*, 587–593.
- (50) Chen, S. Q.; Lopez-Sanchez, P.; Wang, D.; Mikkelsen, D.; Gidley, M. J. Mechanical Properties of Bacterial Cellulose Synthesised by Diverse Strains of the Genus *Komagataeibacter*. *Food Hydrocoll.* **2018**, *81*, 87–95.
- (51) Baccile, N.; Renterghem, L. Van; Griel, P. Le; Ducouret, G.; Brennich, M.; Cristiglio, V.; Roelants, S. L. K. W.; Soetaert, W. Bio-Based Glyco-Bolaamphiphile Forms a Temperature-Responsive Hydrogel with Tunable Elastic Properties. *Soft Matter* **2018**, *14*, 7859–7872.
- (52) Gradzielski, M. Vesicles and Vesicle Gels — Structure and Dynamics of Formation. *J. Phys. Condens. Matter* **2003**, *15*, R655.
- (53) Warriner, H. E.; Idziak, S. H.; Slack, N. L.; Davidson, P.; Safinya, C. R. Lamellar Biogels: Fluid-Membrane-Based Hydrogels Containing Polymer Lipids. *Science* (80-. ). **1996**, *271*, 969–973.
- (54) Ben Messaoud, G.; Griel, P. Le; Prévost, S.; Merino, D. H.; Soetaert, W.; Roelants, S. L. K. W.; Stevens, C. V.; Baccile, N. Single-Molecule Lamellar Hydrogels from Bolaform Microbial Glucolipids. *Soft Matter* **2020**, *16*, 2528–2539.
- (55) Leontidis, E. Investigations of the Hofmeister Series and Other Specific Ion Effects Using Lipid Model Systems. *Adv. Colloid Interface Sci.* **2017**, *243*, 8–22.
- (56) Ji, S.; Xu, L.; Fu, X.; Sun, J.; Li, Z. Light- and Metal Ion-Induced Self-Assembly and Reassembly Based on Block Copolymers Containing a Photoresponsive Polypeptide Segment. *Macromolecules* **2019**, *52*, 4686–4693.
- (57) Chen, L.; Pont, G.; Morris, K.; Lotze, G.; Squires, A.; Serpell, L. C.; Adams, D. J. Salt-Induced Hydrogelation of Functionalised-Dipeptides at High PH. *Chem. Commun.* **2011**, *47*, 12071–12073.
- (58) Cardoso, A. Z.; Mears, L. L. E.; Cattoz, B. N.; Griffiths, P. C.; Schweins, R.; Adams, D. J. Linking Micellar Structures to Hydrogelation for Salt-Triggered Dipeptide Gelators. *Soft Matter* **2016**, *12*, 3612–3621.
- (59) Çelik, E.; Bayram, C.; Akçapinar, R.; Türk, M.; Denkbaş, E. B. The Effect of Calcium Chloride Concentration on Alginate/Fmoc-Diphenylalanine Hydrogel Networks. *Mater.*

*Sci. Eng. C* **2016**, *66*, 221–229.

- (60) Baccile, N.; Cristiglio, V. Primary and Secondary Hydration Forces between Interdigitated Membranes Composed of Bolaform Microbial Glucolipids. *Langmuir* **2020**, *36*, 2191–2198.
- (61) Cui, H.; Muraoka, T.; Cheetham, A. G.; Stupp, S. I. Self-Assembly of Giant Peptide Nanobelts. *Nano Lett.* **2009**, *9*, 945–951.
- (62) Cuvier, A.-S. S.; Berton, J.; Stevens, C. V.; Fadda, G. C.; Babonneau, F.; Van Bogaert, I. N. A. a; Soetaert, W.; Pehau-Arnaudet, G.; Baccile, N. PH-Triggered Formation of Nanoribbons from Yeast-Derived Glycolipid Biosurfactants. *Soft Matter* **2014**, *10*, 3950–3959.
- (63) Teixeira, J. Small-Angle Scattering by Fractal Systems. *J. Appl. Crystallogr.* **1988**, *21*, 781–785.
- (64) Moyer, T. J.; Cui, H.; Stupp, S. I. Tuning Nanostructure Dimensions with Supramolecular Twisting. *J. Phys. Chem. B* **2013**, *117*, 4604–4610.
- (65) Adamcik, J.; Sánchez-Ferrer, A.; Ait-Bouziad, N.; Reynolds, N. P.; Lashuel, H. A.; Mezzenga, R. Microtubule-Binding R3 Fragment from Tau Self-Assembles into Giant Multistranded Amyloid Ribbons. *Angew. Chemie - Int. Ed.* **2016**, *55*, 618–622.
- (66) Raghavan, S. R. Distinct Character of Surfactant Gels: A Smooth Progression from Micelles to Fibrillar Networks. *Langmuir* **2009**, *25*, 8382–8385.
- (67) Pomerantz, W. C.; Yuwono, V. M.; Pizzey, C. L.; Hartgerink, J. D.; Abbott, N. L.; Gellman, S. H. Nanofibers and Lyotropic Liquid Crystals from a Class of Self-Assembling  $\beta$ -Peptides. *Angew. Chemie - Int. Ed.* **2008**, *47*, 1241–1244.
- (68) Ben Messaoud, G.; Le Griel, P.; Hermida-Merino, D.; Roelants, S. L. K. W.; Soetaert, W.; Stevens, C. V.; Baccile, N. PH-Controlled Self-Assembled Fibrillar Network (SAFiN) Hydrogels: Evidence of a Kinetic Control of the Mechanical Properties. *Chem. Mater.* **2019**, *31*, 4817–4830.
- (69) Kim, J.; Park, C. H.; Kim, S. H.; Yoon, S.; Piao, L. Mechanism of Organogel Formation from Mixed-Ligand Silver (I) Carboxylates. *Bull. Korean Chem. Soc.* **2011**, *32*, 3267–3273.
- (70) Westcott, A.; Sumby, C. J.; Walshaw, R. D.; Hardie, M. J. Metallo-Gels and Organogels with Tripodal Cyclotrimeratrylene-Type and 1,3,5-Substituted Benzene-Type Ligands. *New J. Chem.* **2009**, *33*, 902–912.
- (71) Wei, T.; Dang, J.; Lin, Q.; Yao, H.; Liu, Y.; Zhang, W.; Ming, J.; Zhang, Y. Novel Smart Supramolecular Metallo-Hydrogel That Could Selectively Recognize and Effectively

- Remove Pb<sup>2+</sup> in Aqueous Solution. *Sci. China Chem.* **2012**, *55*, 2554–2561.
- (72) Shao, T.; Falcone, N.; Kraatz, H. B. Supramolecular Peptide Gels: Influencing Properties by Metal Ion Coordination and Their Wide-Ranging Applications. *ACS Omega* **2020**, *5*, 1312–1317.
- (73) Li, H.; Yang, P.; Pageni, P.; Tang, C. Recent Advances in Metal-Containing Polymer Hydrogels. *Macromol. Rapid Commun.* **2017**, *38*, 1700109.
- (74) Maire du Poset, A.; Zitolo, A.; Cousin, F.; Assifaoui, A.; Lerbret, A. Evidence for an Egg-Box-like Structure in Iron(II)-Polygalacturonate Hydrogels: A Combined EXAFS and Molecular Dynamics Simulation Study. *Phys. Chem. Chem. Phys.* **2020**, *22*, 2963–2977.
- (75) Maire Du Poset, A.; Lerbret, A.; Boué, F.; Zitolo, A.; Assifaoui, A.; Cousin, F. Tuning the Structure of Galacturonate Hydrogels: External Gelation by Ca, Zn, or Fe Cationic Cross-Linkers. *Biomacromolecules* **2019**, *20*, 2864–2872.
- (76) Huynh, U. T. D.; Lerbret, A.; Neiers, F.; Chambin, O.; Assifaoui, A. Binding of Divalent Cations to Polygalacturonate: A Mechanism Driven by the Hydration Water. *J. Phys. Chem. B* **2016**, *120*, 1021–1032.
- (77) Assifaoui, A.; Lerbret, A.; Uyen, H. T. D.; Neiers, F.; Chambin, O.; Loupiac, C.; Cousin, F. Structural Behaviour Differences in Low Methoxy Pectin Solutions in the Presence of Divalent Cations (Ca<sup>2+</sup> and Zn<sup>2+</sup>): A Process Driven by the Binding Mechanism of the Cation with the Galacturonate Unit. *Soft Matter* **2015**, *11*, 551–560.
- (78) Cui, H.; Cheetham, A. G.; Newcomb, C. J.; Stupp, S. I. Self-Assembling Filament Networks. *Science* (80-. ). **2010**, *555*, 555–560.
- (79) Needleman, D. J.; Ojeda-Lopez, M. A.; Raviv, U.; Miller, H. P.; Wilson, L.; Safinya, C. R. Higher-Order Assembly of Microtubules by Counterions: From Hexagonal Bundles to Living Necklaces. *Proc. Natl. Acad. Sci. U. S. A.* **2004**, *101*, 16099–16103.
- (80) Safinya, C. R.; Raviv, U.; Needleman, D. J.; Zidovska, A.; Choi, M. C.; Ojeda-Lopez, M. A.; Ewert, K. K.; Li, Y.; Miller, H. P.; Quispe, J.; et al. Nanoscale Assembly in Biological Systems: From Neuronal Cytoskeletal Proteins to Curvature Stabilizing Lipids. *Adv. Mater.* **2011**, *23*, 2260–2270.
- (81) Zhang, S.; Greenfield, M. A.; Mata, A.; Palmer, L. C.; Bitton, R.; Mantei, J. R.; Aparicio, C.; De La Cruz, M. O.; Stupp, S. I. A Self-Assembly Pathway to Aligned Monodomain Gels. *Nat. Mater.* **2010**, *9*, 594–601.
- (82) Vand, V.; Aitken, A.; Campbell, R. K. Crystal Structure of Silver Salts of Fatty Acids. *Acta Crystallogr.* **1949**, *2*, 398–403.

- (83) Smith, G.; Sagatys, D. S.; Dahlgren, C.; Lynch, D. E.; Bott, R. C.; Byriel, K. A.; Kennard, C. H. L. Structures of the Silver (I) Complexes with Maleic and Fumaric Acids: Silver(I) Hydrogen Maleate, Silver(I) Maleate and Silver (I) Fumarate. *Zeitschrift für Krist. - New Cryst. Struct.* **1995**, *210*, 44–48.
- (84) Tolochko, B. P.; Chernov, S. V.; Nikitenko, S. G.; Whitcomb, D. R. EXAFS Determination of the Structure of Silver Stearate,  $[\text{Ag}(\text{O}_2\text{C}(\text{CH}_2)_{16}\text{CH}_3)_2]$ , and the Effect of Temperature on the Silver Coordination Sphere. *Nucl. Instruments Methods Phys. Res. Sect. A Accel. Spectrometers, Detect. Assoc. Equip.* **1998**, *405*, 428–434.
- (85) Bairi, P.; Roy, B.; Nandi, A. K. PH and Anion Sensitive Silver(i) Coordinated Melamine Hydrogel with Dye Absorbing Properties: Metastability at Low Melamine Concentration. *J. Mater. Chem.* **2011**, *21*, 11747–11749.
- (86) Xu, F.; Padhy, H.; Al-Dossary, M.; Zhang, G.; Behzad, A. R.; Stingl, U.; Rothenberger, A. Synthesis and Properties of the Metallo-Supramolecular Polymer Hydrogel Poly[Methyl Vinyl Ether-Alt-Mono-Sodium Maleate]·AgNO<sub>3</sub>: Ag<sup>+</sup>/Cu<sup>2+</sup> Ion Exchange and Effective Antibacterial Activity. *J. Mater. Chem. B* **2014**, *2*, 6406–6411.
- (87) Liu, Y.; Ma, W.; Liu, W.; Li, C.; Liu, Y.; Jiang, X.; Tang, Z. Silver(i)-Glutathione Biocoordination Polymer Hydrogel: Effective Antibacterial Activity and Improved Cytocompatibility. *J. Mater. Chem.* **2011**, *21*, 19214–19218.
- (88) Chiad, K.; Stelzig, S. H.; Gropeanu, R.; Weil, T.; Klapper, M.; Muüllen, K. Isothermal Titration Calorimetry: A Powerful Technique to Quantify Interactions in Polymer Hybrid Systems. *Macromolecules* **2009**, *42*, 7545–7552.
- (89) Brautigam, C. A. Fitting Two- and Three-Site Binding Models to Isothermal Titration Calorimetric Data. *Methods* **2015**, *76*, 124–136.
- (90) Fang, Y.; Al-Assaf, S.; Phillips, G. O.; Nishinari, K.; Funami, T.; Williams, P. A.; Li, A. Multiple Steps and Critical Behaviors of the Binding of Calcium to Alginate. *J. Phys. Chem. B* **2007**, *111*, 2456–2462.
- (91) Loh, W.; Brinatti, C.; Tam, K. C. Use of Isothermal Titration Calorimetry to Study Surfactant Aggregation in Colloidal Systems. *Biochim. Biophys. Acta - Gen. Subj.* **2016**, *1860*, 999–1016.
- (92) Sinn, C. G.; Dimova, R.; Antonietti, M. Isothermal Titration Calorimetry of the Polyelectrolyte/Water Interaction and Binding of Ca<sup>2+</sup>: Effects Determining the Quality of Polymeric Scale Inhibitors. *Macromolecules* **2004**, *37*, 3444–3450.
- (93) Lehrmann, R.; Seelig, J. Adsorption of Ca<sup>2+</sup> and La<sup>3+</sup> to Bilayer Membranes: Measurement of the Adsorption Enthalpy and Binding Constant with Titration



- Calorimetry. *BBA - Biomembr.* **1994**, *1189*, 89–95.
- (94) Du, C.; Cai, D.; Qin, M.; Zheng, P.; Hao, Z.; Yin, T.; Zhao, J.; Shen, W. Thermodynamics of Mixed Surfactant Solutions of N, N' - Bis(Dimethyldodecyl)-1,2-Ethanediammoniumdibromide with 1-Dodecyl-3- Methylimidazolium Bromide. *J. Phys. Chem. B* **2014**, *118*, 1168–1179.
- (95) Ito, T. H.; Rodrigues, R. K.; Loh, W.; Sabadini, E. Calorimetric and Light Scattering Investigations of the Transition from Spherical to Wormlike Micelles of C14TAB Triggered by Salicylate. *Langmuir* **2015**, *31*, 6020–6026.
- (96) Johnson, R. A.; Manley, O. M.; Spuches, A. M.; Grosseohme, N. E. Dissecting ITC Data of Metal Ions Binding to Ligands and Proteins. *Biochim. Biophys. Acta* **2016**, *1860*, 892–901.
- (97) Löf, D.; Niemiec, A.; Schillén, K.; Loh, W.; Olofsson, G. A Calorimetry and Light Scattering Study of the Formation and Shape Transition of Mixed Micelles of EO20PO68EO20 Triblock Copolymer (P123) and Nonionic Surfactant (C12EO6). *J. Phys. Chem. B* **2007**, *111*, 5911–5920.
- (98) Bastos-González, D.; Pérez-Fuentes, L.; Drummond, C.; Faraudo, J. Ions at Interfaces: The Central Role of Hydration and Hydrophobicity. *Curr. Opin. Colloid Interface Sci.* **2016**, *23*, 19–28.
- (99) Ringbom, A. *Complexation in Analytical Chemistry*; John Wiley & Sons, Inc.: New York, 1963.
- (100) Katz, A. K.; Glusker, J. P.; Beebe, S. A.; Bock, C. W. Calcium Ion Coordination: A Comparison with That of Beryllium, Magnesium, and Zinc. *J. Am. Chem. Soc.* **1996**, *118*, 5752–5763.
- (101) Carrell, C. J.; Carrell, H. L.; Erlebacher, J.; Glusker, J. P. Structural Aspects of Metal Ion-Carboxylate Interactions. *J. Am. Chem. Soc.* **1988**, *110*, 8651–8656.
- (102) Baes, C. F.; Mesmer, R. E. *The Hydrolysis of Cations*; John Wiley & Sons, Inc.: New York, London, Sydney, Toronto, 1976.
- (103) Lincoln, S. F.; Richens, D. T.; Sykes, A. G. Metal Aqua Ions. In *Comprehensive Coordination Chemistry II*; 2003; pp 515–555.
- (104) Persson, I. Hydrated Metal Ions in Aqueous Solution: How Regular Are Their Structures? *Pure Appl. Chem.* **2010**, *82*, 1901–1917.
- (105) Baccile, N.; Pedersen, J. S.; Pehau-Arnaudet, G.; Van Bogaert, I. N. a. Surface Charge of Acidic Sophorolipid Micelles: Effect of Base and Time. *Soft Matter* **2013**, *9*, 4911–4922.

- (106) Chen, M.; Dong, C.; Penfold, J.; Thomas, R. K.; Smyth, T. J. P.; Perfumo, A.; Marchant, R.; Banat, I. M.; Stevenson, P.; Parry, A.; et al. Influence of Calcium Ions on Rhamnolipid and Rhamnolipid/Anionic Surfactant Adsorption and Self-Assembly. *Langmuir* **2013**, *29*, 3912–3923.
- (107) Baccile, N.; Messaoud, G. Ben; Griel, P. Le; Cowieson, N.; Perez, J.; Geys, R.; Graeve, M. De; Roelants, S. L. K. W.; Soetaert, W. Palmitic Acid Sophorolipid Biosurfactant: From Self-Assembled Fibrillar Network (SAFiN) To Hydrogels with Fast Recovery. *Philos. Trans. A* **2021**, *379*, 20200343.
- (108) Qiao, Y.; Lin, Y.; Wang, Y.; Yang, Z.; Liu, J.; Zhou, J.; Yan, Y.; Huang, J. Metal-Driven Hierarchical Self-Assembled One-Dimensional Nanohelices. *Nano Lett.* **2009**, *9*, 4500–4504.
- (109) Oda, R.; Artzner, F.; Laguerre, M.; Huc, I. Molecular Structure of Self-Assembled Chiral Nanoribbons and Nanotubules Revealed in the Hydrated State. *J. Am. Chem. Soc.* **2008**, *130*, 14705–14712.
- (110) Lis, L. J.; Quinn, P. J.; Collins, J. M. Structures and Mechanisms of Phase Transitions in Surfactant Mixtures: Systems Which Induce the Ribbon Phase. *Mol. Cryst. Liq. Cryst. Inc. Nonlinear Opt.* **1989**, *170*, 119–133.
- (111) Hyde, S. T. Identification of Lyotropic Liquid Crystalline Mesophases. In *Handbook of Applied Surface and Colloid Chemistry*; Holmberg, K., Ed.; John Wiley & Sons, Ltd, 2001; p 299.
- (112) Kelly, S. M.; Jess, T. J.; Price, N. C. How to Study Proteins by Circular Dichroism. *Biochim. Biophys. Acta - Proteins Proteomics* **2005**, *1751*, 119–139.
- (113) Van Workum, K.; Douglas, J. F. Symmetry, Equivalence, and Molecular Self-Assembly. *Phys. Rev. E - Stat. Nonlinear, Soft Matter Phys.* **2006**, *73*, 1–17.
- (114) Parsegian, V. A.; Zemb, T. Hydration Forces: Observations, Explanations, Expectations, Questions. *Curr. Opin. Colloid Interface Sci.* **2011**, *16*, 618–624.
- (115) Stefaniu, C.; Latza, V. M.; Gutowski, O.; Fontaine, P.; Brezesinski, G.; Schneck, E. Headgroup-Ordered Monolayers of Uncharged Glycolipids Exhibit Selective Interactions with Ions. *J. Phys. Chem. Lett.* **2019**, *10*, 1684–1690.
- (116) Dvir, T.; Fink, L.; Asor, R.; Schilt, Y.; Steinar, A.; Raviv, U. Charged Membranes under Confinement Induced by Polymer-, Salt-, or Ionic Liquid Solutions. *Soft Matter* **2013**, *9*, 10640.
- (117) Lotan, O.; Fink, L.; Shemesh, A.; Tamburu, C.; Raviv, U. Critical Conditions for Adsorption of Calcium Ions onto Dipolar Lipid Membranes. *J. Phys. Chem. A* **2016**, *120*,

3390–3396.

- (118) Yaghmur, A.; Laggner, P.; Sartori, B.; Rappolt, M. Calcium Triggered L $\alpha$ -H<sub>2</sub> Phase Transition Monitored by Combined Rapid Mixing and Time-Resolved Synchrotron SAXS. *PLoS One* **2008**, *3*.
- (119) Helfrich, W. Steric Interaction of Fluid Membranes in Multilayer Systems. *Z. Naturforsch* **1978**, *33a*, 305–315.
- (120) Monzel, C.; Sengupta, K. Measuring Shape Fluctuations in Biological Membranes. *J. Phys. D. Appl. Phys.* **2016**, *49*, 243002.
- (121) Gupta, S.; Mel, J. U. De; Schneider, G. J. Dynamics of Liposomes in the Fluid Phase. *Curr. Opin. Colloid Interface Sci.* **2019**, *42*, 121.
- (122) Nagao, M.; Chawang, S.; Hawa, T. Interlayer Distance Dependence of Thickness Fluctuations in a Swollen Lamellar Phase. *Soft Matter* **2011**, *7*, 6598–6605.

## Supporting information

### **Ca<sup>2+</sup> and Ag<sup>+</sup> orient low-molecular weight amphiphile self-assembly into “nano-fishnet” fibrillar hydrogels with unusual $\beta$ -sheet-like raft domains**

Alexandre Poirier,<sup>a</sup> Patrick Le Griel,<sup>a</sup> Ingo Hoffmann,<sup>b</sup> Javier Perez,<sup>c</sup> Petra Pernot,<sup>d</sup> Jérôme Fresnais,<sup>e</sup> Niki Baccile<sup>a,\*</sup>

<sup>a</sup> Sorbonne Université, Centre National de la Recherche Scientifique, Laboratoire de Chimie de la Matière Condensée de Paris, LCMCP, F-75005 Paris, France

<sup>b</sup> Institut Laue-Langevin, 38042 Grenoble, France

<sup>c</sup> Synchrotron Soleil, L'Orme des Merisiers, Saint-Aubin, BP48, 91192 Gif-sur-Yvette Cedex, France

<sup>d</sup> ESRF – The European Synchrotron, CS40220, 38043 Grenoble, France

<sup>e</sup> Sorbonne Université, CNRS, Laboratoire de Physico-chimie des Électrolytes et Nanosystèmes Interfaciaux, PHENIX - UMR 8234, F-75252, Paris Cedex 05, France

\* Corresponding author:

Dr. Niki Baccile

E-mail address: niki.baccile@sorbonne-universite.fr

Phone: +33 1 44 27 56 77

## Experimental

*Neutron spin echo (NSE).* Neutron Spin-Echo (NSE)<sup>1</sup> measurements have been performed at the instrument IN15<sup>2</sup> at the Institut Laue-Langevin (ILL) in Grenoble (France). Four different wavelengths ( $\lambda$ ) have been used, namely 13.5, 12, 10 and 8 Å allowing to reach maximum Fourier times  $t$  of 477, 335, 194 and 99 ns, respectively and covering a  $q$ -range from 0.03 to 0.14 Å<sup>-1</sup>, where  $q = \frac{4\pi}{\lambda} \sin(\frac{\theta}{2})$  is the modulus of the scattering vector, with scattering angle  $\theta$ . The data were corrected for resolution effects using graphite and the scattering from the aqueous background was subtracted. Experiments were performed in a fully deuterated (D<sub>2</sub>O) medium.

To analyze the data, the Zilman-Granek model<sup>3</sup> was applied. Starting from a Helfrich bending Hamiltonian,<sup>4</sup> it predicts a stretched exponential shape of the intermediate scattering function  $S(q, t)$  (Eq. 1) with a stretch exponential  $\beta = 2/3$ ,  $I(q, t)$  being the spin echo intensity at a given value of  $q$  and time,  $t$

$$\frac{I(q, t)}{I(q, 0)} = S(q, t) = e^{-(\Gamma_{ZG} t)^\beta} \quad \text{Eq. S1}$$

where

$$\Gamma_{ZG} = \alpha \gamma \left( \frac{k_b T}{\kappa} \right)^{\frac{1}{2}} \left( \frac{k_b T}{\eta} \right) q^3 \quad \text{Eq. S2}$$

from which, the scaled bending rigidity,  $\kappa$ , is

$$\frac{\kappa}{k_b T} = \left( \frac{\alpha \gamma}{\eta} (k_b T)^{\frac{1}{2}} \frac{q^3}{\Gamma_{ZG}} \right)^2 \quad \text{Eq. S3}$$

where  $\alpha$  is a prefactor,  $\gamma \approx 1$  for  $\frac{k_b T}{\kappa} \ll 1$ ,  $\eta$  is the solvent viscosity (generally  $\eta(\text{D}_2\text{O}) = 1.1 \cdot 10^{-3}$  Pa.s at 25°C),  $k_b$  is the Boltzmann constant,  $T$  is the temperature in Kelvin.

*Small angle X-ray scattering (SAXS).* SAXS experiments have been performed on various beamlines and synchrotron facilities. The environments as well as the samples associated to each session are presented below.

*Capillary SAXS.* SAXS experiments are performed using hydrogel samples prepared at room temperature and analyzed into 1.5 mm quartz capillaries on the Swing beamline (proposal N° 20201747) at Soleil Synchrotron (Saint-Aubin, France) and on the BM29 beamline at the ESRF Synchrotron (Grenoble, France). Samples are manually injected into the capillary using a 1.0

mL syringe. The Swing beamline is used with an energy of  $E = 12$  keV and a fixed sample-to-detector (Eiger 4M - Dectris) distance of 2.005 m. An additional run has also been performed on the SWING beamline (proposal Number: BAG 20201118), with  $E = 12$  keV and two sample-to-detector distances, 6.60 m and 0.50 m.

The BM29 beamline (Proposal N° MX 2311) is used with an energy of  $E = 12.5$  KeV and a sample-to-detector distance of 2.83 m.  $q$  is the wave vector, with  $q = 4\pi/\lambda \sin(\theta)$ ,  $2\theta$  corresponding to the scattering angle and  $\lambda$  the wavelength. The  $q$ -range is calibrated between  $\sim 0.05 < q / \text{nm}^{-1} < \sim 5$ , using the standard silver behenate calibrant ( $d_{(001)} = 58.38 \text{ \AA}$ ); raw data obtained on the 2D detector are integrated azimuthally using the in-house software provided at the beamline and thus to obtain the typical scattered intensity  $I(q)$  profile. Absolute intensity units are determined by measuring the scattering signal of water ( $I(q=0) = 0.0163 \text{ cm}^{-1}$ ).

| Figure      | Sample  | Experiment     | Beamline | Synchrotron | Proposal N°  |
|-------------|---|----------------|----------|-------------|--------------|
| 3a, 3b      | {Ca <sup>2+</sup> }G-C18:1, no shear  | Capillary SAXS | SWING    | Soleil      | BAG 20201118 |
| 3a, 3b      | {Ca <sup>2+</sup> }G-C18:1 shear<br>{Ca <sup>2+</sup> }G-C18:1, no shear<br>G-C18:1 | Capillary SAXS | BM29     | ESRF        | MX 2311      |
| 3a          | {Ag <sup>+</sup> }G-C18:1 shear   | Capillary SAXS | SWING    | Soleil      | 20201747     |
| S 1, S 4a,b | All   | Capillary SAXS | BM29     | ESRF        | MX 2311      |
| S 5         | pH 8  | Capillary SAXS | BM29     | ESRF        | MX 2311      |

*Cryogenic-transmission electron microscopy (Cryo-TEM).* Pictures are recorded on an FEI Tecnai 120 twin microscope operating at 120 kV with an Orius 1000 CCD numeric camera. The sample holder is a Gatan Cryo holder (Gatan 626DH, Gatan). Digital Micrograph software is used for image acquisition. Cryo-fixation is done with low dose on a homemade cryo-fixation device. The solutions are deposited on a glow-discharged holey carbon coated TEM nickel grid (Quantifoil R2/2, Germany). Excess solution is removed and the grid is immediately plunged into liquid ethane at  $-180^\circ\text{C}$  before transferring them into liquid nitrogen. All grids are kept at liquid nitrogen temperature throughout all experimentation. Cryo-TEM images are treated and analyzed using Fiji software, available free of charge at the developer's web site.<sup>5</sup>

*Isothermal titration calorimetry (ITC).* ITC experiments are performed using a nano-ITC from TA Instruments. A water solution is prepared at pH 8 and used as solvent by G-C18:1. Note that a classical phosphate buffer solution could not be used due to a side reaction with

calcium. All solutions are degassed during 20 min under vacuum (400 mmHg). The titration experiments between calcium chloride, or silver nitrate, and G-C18:1 employ a solution at pH 8 of calcium chloride as titrant at concentration of 80 et 50 mM. The titrated solution corresponds to 20 mM of G-C18:1 at pH in water, freshly prepared before the experiment to prevent precipitation of calcium hydroxide. Experiments are run at 23°C, 25 injections of 10  $\mu$ L of titrant each every 300 s. To take account of dilution effects, all titration experiments are followed by the same experiment without G-C18:1 in water at pH 8, which is used as a control, subtracted to the original titration measurement. The mixing rotation of the syringe was established to 200 rpm.

Data are fitted using a multi-site model using Nano-data analysis software (TA Instruments) in order to determine the thermodynamic as well as the reaction parameters of the interaction between  $\text{Ca}^{2+}$  and G-C18:1. From the enthalpy ( $\Delta H$ ) and the binding constant ( $K_a$ ) of the reaction, the entropy ( $\Delta S$ ) and the Gibbs free energy ( $\Delta G$ ) of reaction were calculated using the equation  $\Delta G = \Delta H - T\Delta S = -RT \cdot \ln(K_a)$ . For the titration of  $\text{Ag}^+$  and G-C18-1, an independent model is used, as a single reaction is observed.

*Solid-state nuclear magnetic resonance (ssNMR).*  $^{13}\text{C}$  solid-state NMR experiments were carried out on an Avance III HD Bruker 7.05 T ( $\nu_{\text{H}} = 300$  MHz) spectrometer and a 4 mm magic angle spinning (MAS) probe. The  $^{13}\text{C}$  NMR spectra were obtained by  $^1\text{H} \rightarrow ^{13}\text{C}$  cross-polarization (CP) under magic angle spinning (MAS).  $\nu_{\text{MAS}} = 10$  kHz, number of transients, NS = 1024; time domain size, TD = 2 k; pulse length,  $p(^1\text{H}) = 7.00$   $\mu\text{s}$ ,  $p(^{13}\text{C}) = 3.62$   $\mu\text{s}$ , relaxation delay, D = 3 s; CP is performed under ramped (square) conditions with contact time during CP,  $t_c$  being indicated in the main text.

**Table S 1 – Literature survey based on the scattering (SAXS or SANS) data reported in each cited article. Articles cited under *SAFiN with disordered fibers* report a typical scattering profile of the fiber alone, with or without a structure peak. Articles cited under *SAFiN with suprafibrillar assembly* report scattering profiles where the fiber’s form factor is superimposed with the structure factor associated to the 3D organization of the fibers. Articles cited under  *$\beta$ -sheet-like gel (“nano-fishnet”)* report those hydrogels characterized by entanglement and  $\beta$ -sheet or  $\beta$ -sheet-like structure.**

| <b>SAFiN with disordered fibers</b>                       |                   |
|---|-------------------|
| Not gelled  | 6–9               |
| Gels  | 10,11,20–22,12–19 |
| <b>SAFiN with suprafibrillar assembly</b>                 |                   |
| Hexagonal bundles/Columnar hexagonal                      | 23–28             |
| Raft-like/lamellar (solution, not gelled)                 | 29,30             |
| <b><math>\beta</math>-sheet-like gel (“nano-fishnet”)</b> |                   |
| Biopolymers (fibroin, actin)                              | 31–38             |
| SAFiN   | This work         |



**Table S 2 - Table of correlation peaks related to SAXS data presented in Figure 3 in the main text. a) Correlation peaks of 3 wt% G-C18:1 at basic pH and  $[\text{Ca}^{2+}]/[\text{G-C18:1}] = 0.61$ . b) Correlation peaks of 3 wt% G-C18:1 at basic pH with  $[\text{Ag}^+]/[\text{G-C18:1}] = 1.0$ .**

$[\text{Ca}^{2+}]/[\text{G-C18:1}] = 0.61$ ,  $C_{\text{G-C18:1}} = 3 \text{ wt}\%$

| Sheared gel |                             |            | Static gel |                             |       |
|-------------|-----------------------------|------------|------------|-----------------------------|-------|
| Peak        | position / $\text{nm}^{-1}$ | ratio      | Peak       | position / $\text{nm}^{-1}$ | ratio |
| $q_{f1}$    | 2.41                        | -          | 1          | 0.62                        | 1     |
| $q_{f2}$    | 3.02                        | 1.25       | 2          | 1.35                        | 2.2   |
| $q_{f3}$    | 4.71                        | $\sqrt{2}$ | 3          | 1.81                        | 2.9   |
|             |                             |            | 4          | 2.48                        | 4.0   |
|             |                             |            | 5          | 3.18                        | 5.1   |
|             |                             |            | 6          | 3.73                        | 6.0   |
|             |                             |            | 7          | 4.49                        | 7.2   |
|             |                             |            | 8          | 4.88                        | 7.9   |
|             |                             |            | 9          | 5.68                        | 9.2   |

$[\text{Ag}^+]/[\text{G-C18:1}] = 1$ ,  $C_{\text{G-C18:1}} = 3 \text{ wt}\%$

| Peak | position / $\text{nm}^{-1}$ | ratio |
|------|-----------------------------|-------|
| 1    | 1.18                        | 1     |
| 2    | 2.40                        | 2.03  |
| 3    | 3.52                        | 2.98  |
| 4    | 4.74                        | 4.02  |

a)

b)

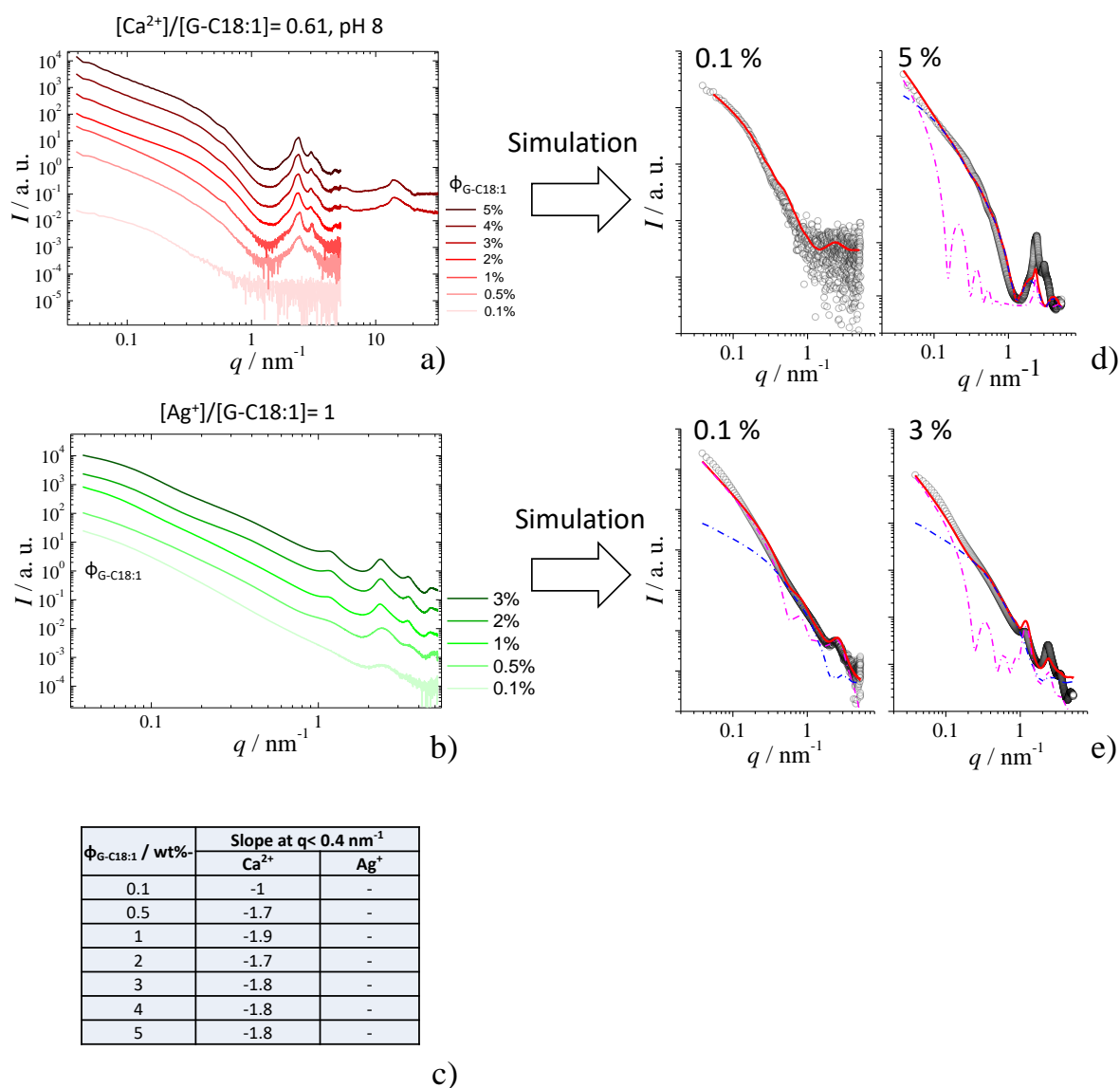


**Figure S 1 – SAXS profiles recorded as a function of G-C18:1 concentration at basic pH for a) {Ca<sup>2+</sup>}G-C18:1 and b) {Ag<sup>+</sup>}G-C18:1 gels. Table in c) illustrates the log(I)-log(q) dependency (slope) for the Ca<sup>2+</sup> system. The slopes for the Ag<sup>+</sup> cannot be reasonably estimated due to the overlap of two scattering signals below about 0.2 nm<sup>-1</sup>. d-e) Simulated SAXS curves extracted from the experiments in a-b): {Ca<sup>2+</sup>}G-C18:1 (0.1 wt%, 5 wt%) and {Ag<sup>+</sup>}G-C18:1 (0.1 wt%, 3 wt%). Magenta segmented curves employ model *M1*; blue segmented curves employ model *M2*; red solid curve employ the sum of *M1* and *M2*. Simulation was performed with form factor models available in SasView 3.1.2 software. The full list of parameters and model description is given in Table S 3 and Page S 8 to Page S 10 in the Supporting Information.**

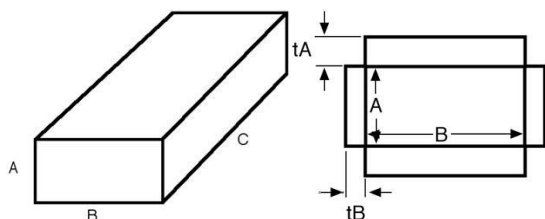
**Table S 3 – Set of the numerical parameters used for the form factor models employed to simulate SAXS curves of {Ca<sup>2+</sup>}G-C18:1 (0.1 wt%, 5 wt%) and {Ag<sup>+</sup>}G-C18:1 (0.1 wt%, 3 wt%). Simulations are shown in Figure S 1d,e: magenta segmented curves employ model *M1*; blue segmented curves employ model *M2*; red solid curve employ the sum of *M1* and *M2*.**

*M1* (core-shell parallelepiped model) and *M2* (lamellar paracrystal model) are shortly described below.

| <b>{Ca<sup>2+</sup>}G-C18:1</b><br>[Ca <sup>2+</sup> ]/[G-C18:1]= 0.61, pH 8   |  |
|--|--|
| 0.1 wt%  | 5 wt%  |
| <i>M1</i> _background = 0.00003 1/cm<br><i>M1</i> _longC = 100 nm<br><i>M1</i> _midB = 30 nm<br><i>M1</i> _rimA = 1 nm<br><i>M1</i> _rimB = 0 nm<br><i>M1</i> _rimC = 0 nm<br><i>M1</i> _scale = 0.05<br><i>M1</i> _shortA = 2.6 nm<br><i>M1</i> _sld_pcore = 8.0e-04 1/nm <sup>2</sup><br><i>M1</i> _sld_rimA = 1.6e-03 1/nm <sup>2</sup><br><i>M1</i> _sld_rimB = -<br><i>M1</i> _sld_rimC = -<br><i>M1</i> _sld_solv = 9.4e-04 1/nm <sup>2</sup>  | <i>M1</i> _background = 0.3 1/cm<br><i>M1</i> _longC = 100 nm<br><i>M1</i> _midB = 25 nm<br><i>M1</i> _rimA = 1.45 nm<br><i>M1</i> _rimB = 0 nm<br><i>M1</i> _rimC = 0 nm<br><i>M1</i> _scale = 10000<br><i>M1</i> _shortA = 3.3 nm<br><i>M1</i> _sld_pcore = 8.0e-04 1/nm <sup>2</sup><br><i>M1</i> _sld_rimA = 1.8e-03 1/nm <sup>2</sup><br><i>M1</i> _sld_rimB = -<br><i>M1</i> _sld_rimC = -<br><i>M1</i> _sld_solv = 9.4e-06 1/nm <sup>2</sup><br><i>M2</i> _background = 0.3 1/cm<br><i>M2</i> _Nlayers = 15<br><i>M2</i> _pd_spacing = 0.1<br><i>M2</i> _scale = 500<br><i>M2</i> _sld_layer = 11.5e-04 1/nm <sup>2</sup><br><i>M2</i> _sld_solvent = 9.4e-04 1/nm <sup>2</sup><br><i>M2</i> _spacing = 2.7 nm<br><i>M2</i> _thickness = 0.5 nm<br>scale_factor = 1 |
| <b>{Ag<sup>+</sup>}G-C18:1</b><br>[Ag <sup>+</sup> ]/[G-C18:1]= 1, pH 8  |  |
| 0.1 wt%  | 3 wt%  |
| <i>M1</i> _background = 0.00005 1/cm<br><i>M1</i> _longC = 100 nm<br><i>M1</i> _midB = 10 nm<br><i>M1</i> _rimA = 1 nm<br><i>M1</i> _rimB = 0 nm<br><i>M1</i> _rimC = 0 nm<br><i>M1</i> _scale = 0.1<br><i>M1</i> _shortA = 2.8 nm<br><i>M1</i> _sld_pcore = 3e-04 1/nm <sup>2</sup><br><i>M1</i> _sld_rimA = 11e-04 1/nm <sup>2</sup><br><i>M1</i> _sld_rimB = -<br><i>M1</i> _sld_rimC = -<br><i>M1</i> _sld_solv = 9.4e-04 1/nm <sup>2</sup><br><i>M2</i> _background = 0 1/cm<br><i>M2</i> _Nlayers = 5<br><i>M2</i> _pd_spacing = 0.25<br><i>M2</i> _scale = 2.9<br><i>M2</i> _sld_layer = 11e-04 1/nm <sup>2</sup><br><i>M2</i> _sld_solvent = 9.4e-04 1/nm <sup>2</sup><br><i>M2</i> _spacing = 2.2 nm<br><i>M2</i> _thickness = 1 nm<br>scale_factor = 1 | <i>M1</i> _background = 0.4 1/cm<br><i>M1</i> _longC = 100 nm<br><i>M1</i> _midB = 10 nm<br><i>M1</i> _rimA = 1 nm<br><i>M1</i> _rimB = 0 nm<br><i>M1</i> _rimC = 0 nm<br><i>M1</i> _scale = 310<br><i>M1</i> _shortA = 2.8 nm<br><i>M1</i> _sld_pcore = 4e-06 1/nm <sup>2</sup><br><i>M1</i> _sld_rimA = 20e-06 1/nm <sup>2</sup><br><i>M1</i> _sld_rimB = -<br><i>M1</i> _sld_rimC = -<br><i>M1</i> _sld_solv = 9.4e-04 1/nm <sup>2</sup><br><i>M2</i> _background = 0.008 1/cm<br><i>M2</i> _Nlayers = 5<br><i>M2</i> _pd_spacing = 0.13<br><i>M2</i> _scale = 1000<br><i>M2</i> _sld_layer = 11.6e-04 1/nm <sup>2</sup><br><i>M2</i> _sld_solvent = 9.4e-04 1/nm <sup>2</sup><br><i>M2</i> _spacing = 5.1 nm<br><i>M2</i> _thickness = 0.5 nm<br>scale_factor = 1      |

Simulations were performed with form factor models available in the software SasView 3.1.2.<sup>39</sup> Full model description can be found in the documentation of SasView,<sup>39</sup> while a short description follows.

\* *Model, M1, CSParallelepipedModel*: Calculates the form factor for a rectangular solid with a core-shell structure. The thickness and the scattering length density of the shell or “rim” can be different on all three (pairs) of faces.



\* *Model, M2, LamellarPCrystalModel*: This model calculates the scattering from a stack of repeating lamellar structures. The stacks of lamellae (infinite in lateral dimension) are treated as a paracrystal to account for the repeating spacing.

The choice of *M1* and *M2*, as well as the parameters listed in Table S 3, was based on the knowledge of the system, estimated by the chemical structure of G-C18:1 and cryo-TEM data presented in the main text. From cryo-TEM, one observes fibers with a flat cross-section. On the other hand, previous modelling of SAXS profiles characterizing the self-assembly of G-C18:1 required the use of a core-shell model.<sup>40</sup> For this reason, we selected a core-shell parallelepiped form factor model (*M1*). *M1* reveals to be particularly efficient in modelling the SAXS profile of {Ca<sup>2+</sup>}G-C18:1 under diluted conditions at 0.1 wt% (Figure S 1d), where fibers do not interact with each other. On the other hand, all other samples could only be modelled with a second contribution, namely a lamellar paracrystal (*M2*). Employing *M2* is justified by the cryo-TEM images in the main text, which show the assembly of the fibers into lamellar rafts. Lamellar rafts contribute both to the low-q scattering as a flat morphology but also to the lamellar structure factor at mid-q/high-q. Unfortunately, SasView does not provide any valuable structure factor allowing simulation of the diffraction peaks found in {Ca<sup>2+</sup>}G-C18:1 at 3 wt%.

The list of the parameters given in Table S 3 is given hereafter and discussed below.

Form factor for a rectangular Shell. Below are the Parameters.

scale: scale factor

shortA: length of short edge [A]

midB: length of another short edge [A]

longC: length of long edge of the parallelepiped [A]

rimA: length of short edge [A]

rimB: length of another short edge [A]

rimC: length of long edge of the parallelepiped [A]

sld\_rimA: sld of rimA [ $1/\text{\AA}^2$ ]

sld\_rimB: sld of rimB [ $1/\text{\AA}^2$ ]

sld\_rimC: sld of rimC [ $1/\text{\AA}^2$ ]

sld\_core: Pipe\_sld [ $1/\text{\AA}^2$ ]

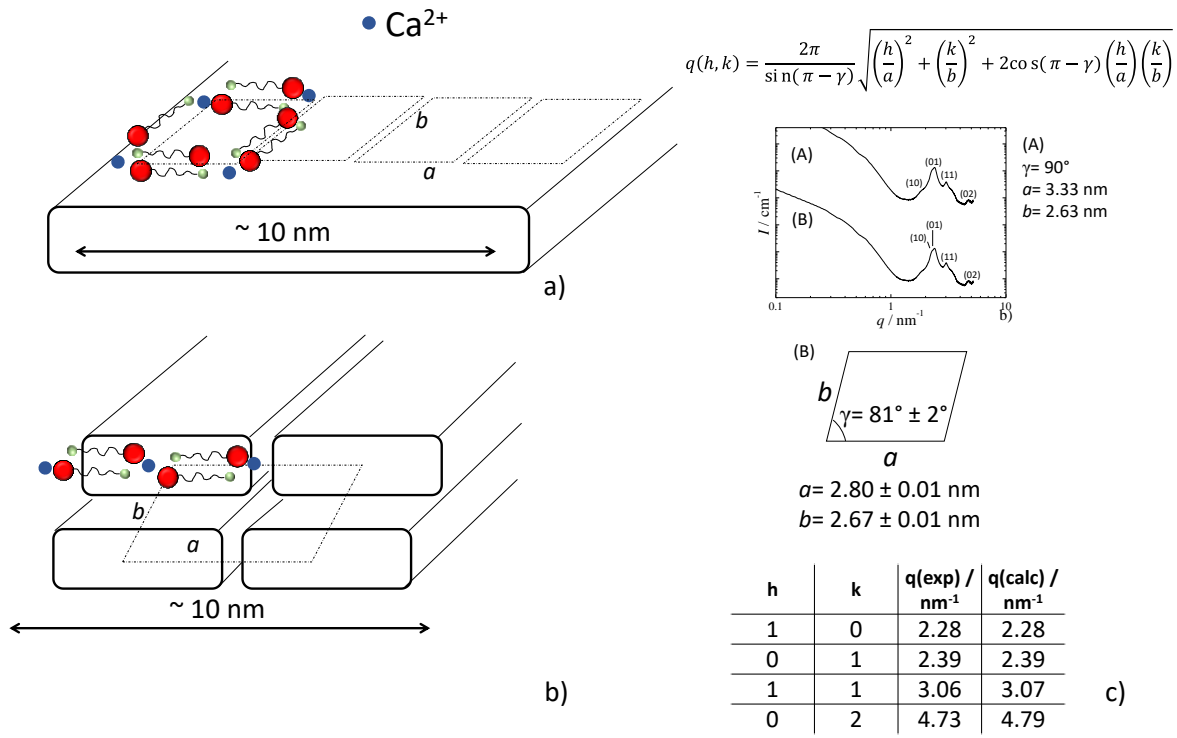
sld\_solv: solvent\_sld [ $1/\text{\AA}^2$ ]

background: incoherent Background [1/cm]

[Lamellar ParaCrystal Model] Parameter Definitions: scale = scale factor,  
background = incoherent background  
thickness = lamellar thickness,  
sld\_layer = layer scattering length density,  
sld\_solvent = solvent scattering length density.  
Nlayers = no. of lamellar layers  
spacing = spacing between layers  
pd\_spacing = polydispersity of spacing

Parameters were accurately selected to keep the physics of the model as close as possible to the experimental data. For instance, the value of  $9.4 \cdot 10^{-4} \text{ 1/nm}^2$  for the sld (scattering length density) of the solvent reflects the value for water. The sld of the core, classically in the order of  $8 \cdot 10^{-4} \text{ 1/nm}^2$  for a hydrocarbon, was tentatively modified only if necessary, and possibly reflecting the higher contrast between the core, the shell and the solvent. Some parameters did not have any influence, like the size of the rim B and rim C. These were set to zero. The length of the C axis is also not important, provided it is sufficiently long. The arbitrary value of 100 nm chosen here was satisfactory for the simulation. Other parameters were, on the contrary, critical and were adapted manually with extreme care. In *M1*, these are the B and A sides, the rim of A, the sld of the A-rim. In *M2*, these are the spacing, the polydispersity of the spacing, the number of layers and the thickness. The choice of the scale was always arbitrary.

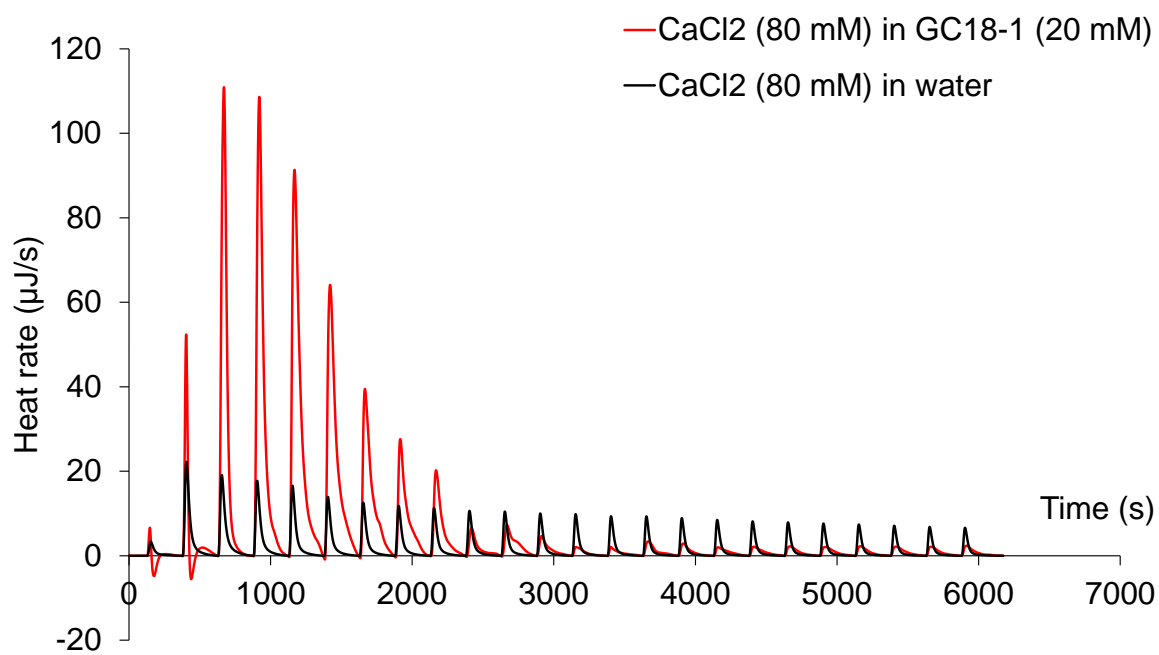
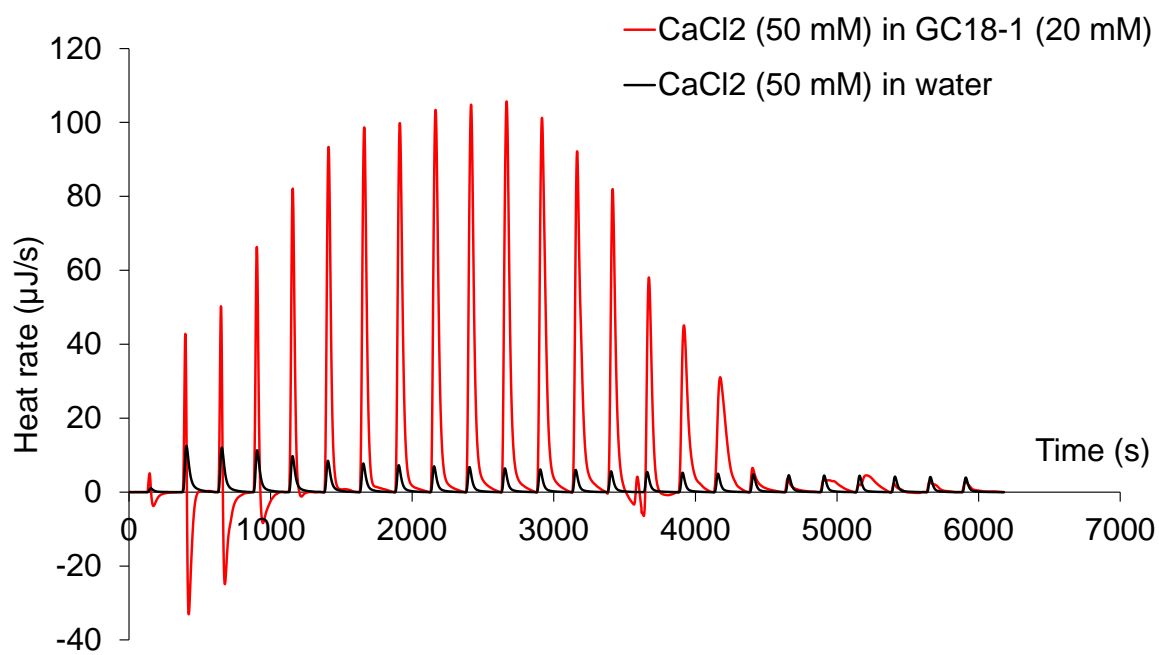
Please note that the values given in Table S 3 are indicative of an order of magnitude and should not be taken as accurate. These were optimized manually for the purpose of the simulation but they are not the result of a numerical fitting process, which revealed to be too complex, due to the large number of critical free variables.



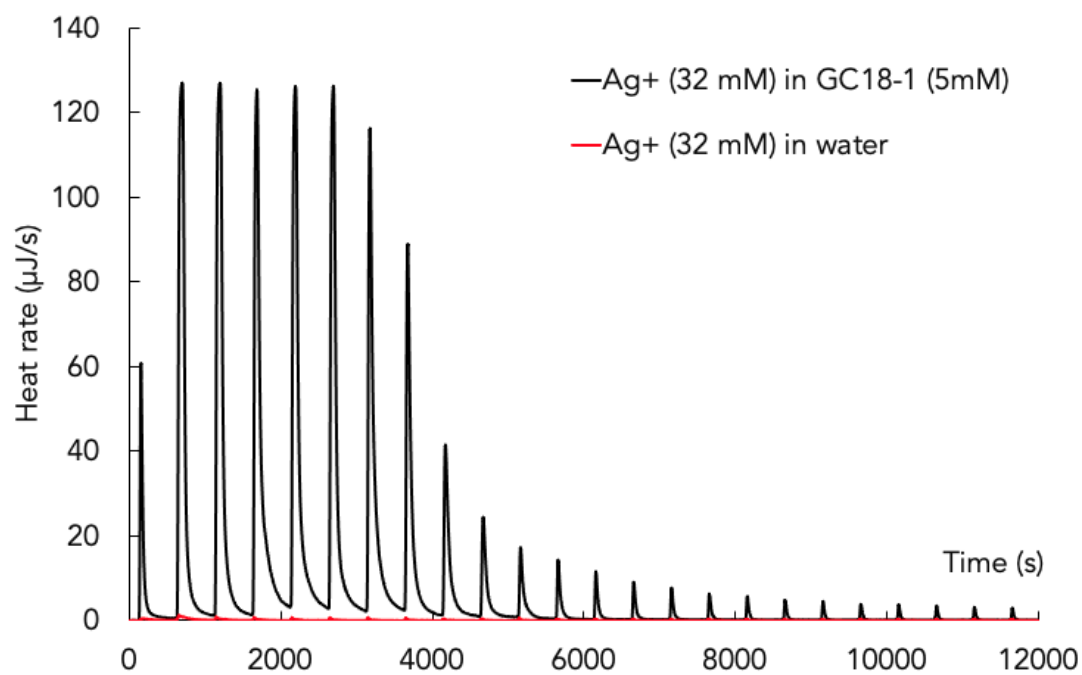
**Figure S 2 –Possible arrangements of  $\text{Ca}^{2+}$  and G-C18:1 within an oblique lattice either a) within (according to ref. <sup>41,42</sup>) or b) orthogonal (ribbon phase<sup>43,44</sup>) to the fiber's longitudinal axis. c) (A) and (B) show the possible attributions of the Bragg peaks typically found in sheared  $\{\text{Ca}^{2+}\}$ G-C18:1 samples.**

Figure S 2 shows the tentative attribution of the peaks and evaluation of the fiber's structure. First of all, one could pinpoint the main peaks at  $q_1 = 2.41 \text{ nm}^{-1}$ ,  $q_2 = 3.02 \text{ nm}^{-1}$  and  $q_3 = 4.71 \text{ nm}^{-1}$ , identifying a ratio of  $q_2/q_1 = 1.25$  and  $q_3/q_1 = 1.95$  ( $\sim 2$ ). Many similar SAFiN systems only show one main structural peak corresponding to an inter-lipid distance,<sup>9,45</sup> or an hexagonal order ( $1 : \sqrt{3} \equiv 1.73 : 2$ ) within the fiber (Table S 1). However, the peak positional ratio  $q_2/q_1 = 1.25$  found here is quite atypical. If such ratio certainly excludes any lamellar and hexagonal arrangement, as well as all cubic phases due to the strong anisotropy of the fibers, two other possibilities exist. In the first one, one could suppose a ribbon mesophase with a rectangular, or oblique, 2D lattice orthogonal to the fiber's longitudinal axis (Figure S 2b);<sup>43,44</sup> in the second one, one could suppose a flat ribbon with a rectangular, or oblique, crystalline arrangement of the lipids within the fiber's plane (Figure S 2a).<sup>41,42</sup> The values of calculated wavevectors,  $q(\text{calc})$ , match well the experimental data,  $q(\text{exp})$ , as shown in Figure S 2b, when a 2D rectangular/oblique lattice with  $(h, k) = 1, 0; 0, 1; 1, 1; 0, 2$  is employed. However, the rectangular lattice ( $\gamma = 90^\circ$ , hypothesis (A) in Figure S 2b) requires indexing the broad shoulder at  $1.8 \text{ nm}^{-1}$  as the  $(1, 0)$  plane. Although not impossible, this hypothesis seems to be inconsistent when

considering the peak width, much broader for (1,0) than for all other reflections. On the contrary, the use of an oblique lattice requires indexing of the multicomposite peak at about  $2.40 \text{ nm}^{-1}$  (hypothesis (B) in Figure S 2b). For this hypothesis, the broad shoulders at  $1.8 \text{ nm}^{-1}$  and  $3.5 \text{ nm}^{-1}$  could be attributed to the subjacent oscillation of the form factor. Possibly, one last hypothesis could leave room for interpreting the data as a combination of coexisting polymorphs with similar periods, as recently proposed for comparable glycolipid fibrillary hydrogels.<sup>46,47</sup> Finally, a broad peak is observed at  $13.9 \text{ nm}^{-1}$  (Figure S 1a), corresponding to a d-spacing of  $0.45 \text{ nm}$ , compatible with an intra-alkyl chain distance, generally poorly affected by molecular packing.<sup>48,49</sup> Although important, a detailed study of the crystal structure of SAFiN is a task *per se* and out of the scope of this work.







**Figure S 3 – Calorimetric titrations (24 injections of 10  $\mu\text{L}$  each) of a G-C18:1 solution (20 mM) with a solution of 50 mM of 80 mM  $\text{CaCl}_2$ . Calorimetric titrations (24 injections of 10  $\mu\text{L}$  each) of a G-C18:1 solution (5 mM) with a solution of 32 mM  $\text{AgNO}_3$ .**

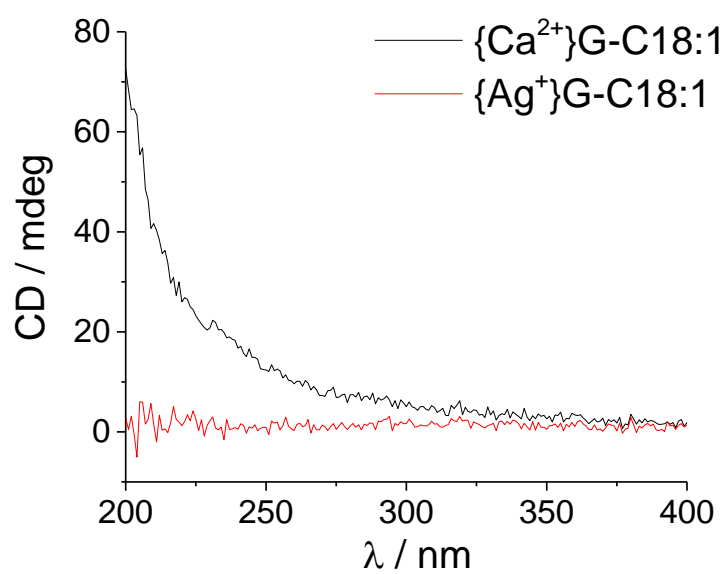


**Figure S 4 – Circular dichroism spectra recorded on typical  $\{Ag^{+}\}G-C8:1$  and  $\{Ca^{2+}\}G-C18:1$  gels prepared at 3 wt% in water.**

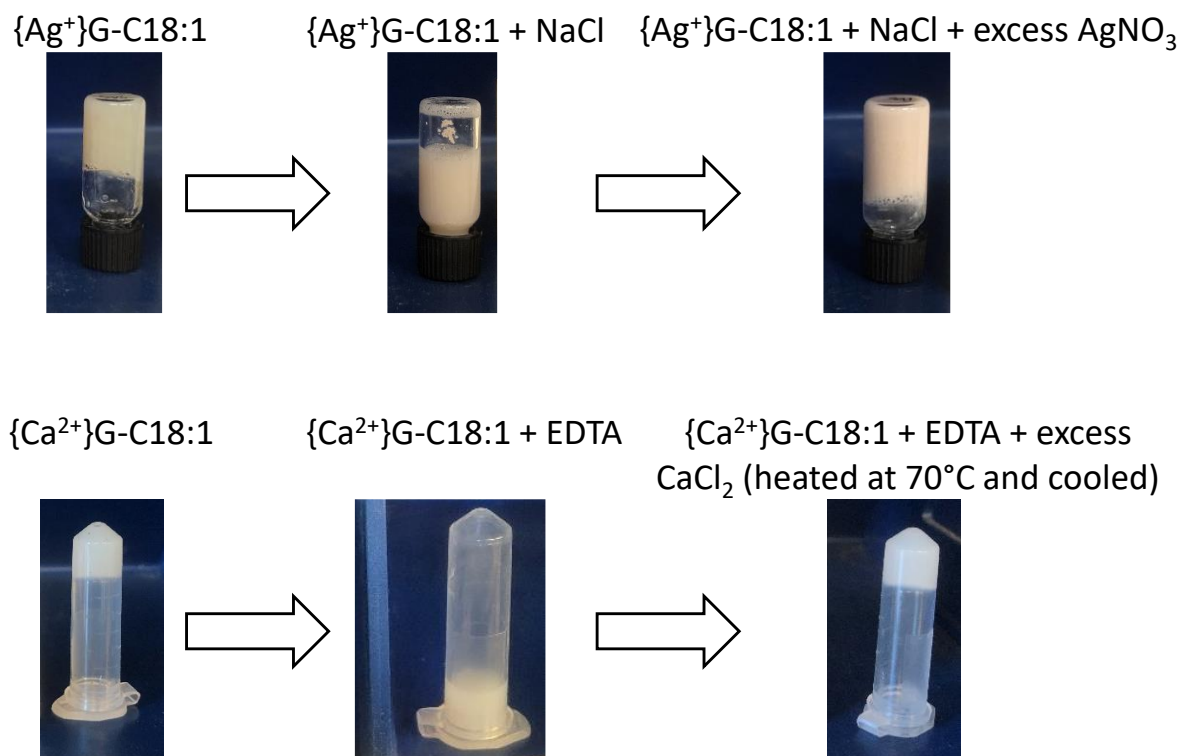


**Figure S 5 – Stability and reversibility tests employing ethylenediaminetetraacetate (EDTA) and NaCl.** EDTA complexes  $\text{Ca}^{2+}$  ions and it is employed with  $\{\text{Ca}^{2+}\}\text{G-C18:1}$  gels, while NaCl precipitates silver ion as AgCl and it is used with  $\{\text{Ag}^+\}\text{G-C18:1}$  gels (gel volume 1 mL). For  $\{\text{Ag}^+\}\text{G-C18:1}$ , we sequentially employ:  $\text{C}_{\text{G-C18:1}} = 3 \text{ wt\%}$  at pH 10 with  $[\text{AgNO}_3] = 65.2 \text{ mM} \rightarrow$  a gel forms.  $[\text{NaCl}] = 65.2 \text{ mM}$  destabilizes the gel.  $[\text{AgNO}_3] = 130.4 \text{ mM}$  are added and the gel forms again. For  $\{\text{Ca}^{2+}\}\text{G-C18:1}$ , we sequentially employ:  $\text{C}_{\text{G-C18:1}} = 3 \text{ wt\%}$  at pH 10 with  $[\text{CaCl}_2] = 40.0 \text{ mM} \rightarrow$  a gel forms (gel volume 500  $\mu\text{L}$ ). 4  $\mu\text{L}$  of a saturated EDTA solution destabilizes the gel into a liquid sol and reduces pH to 5.9.  $[\text{CaCl}_2] = 80.0 \text{ mM}$  are added  $\rightarrow$  the solution is still liquid.  $[\text{NaOH}] = 40 \text{ mM}$ , pH raises from 6.7 to  $\geq 10 \rightarrow$  the solution still liquid. Heating at 70°C during 5 min and cooling at room temperature  $\rightarrow$  a gel forms.

## References

1. Mezei, F. Neutron spin echo. in *Lecture Notes in Physics* (ed. Mezei, F.) 1–26 (Springer, 1980).
2. Farago, B. *et al.* The in15 upgrade. *Neutron News* **26**, 15 (2015).
3. Zilman, A. G. & Granek, R. Undulations and dynamic structure factor of membranes. *Phys. Rev. Lett.* **77**, 4788 (1996).
4. Helfrich, W. Elastic Properties of Lipid Bilayers - Theory and Possible Experiments. *Z. Naturforsch* **28**, 693–703 (1973).
5. Schindelin, J. *et al.* Fiji: an open-source platform for biological-image analysis. *Nat. Methods* **9**, 676–682 (2012).
6. Besenius, P. *et al.* Controlling the growth and shape of chiral supramolecular polymers in water. *Proc. Natl. Acad. Sci. U. S. A.* **107**, 17888–17893 (2010).
7. Adamcik, J. *et al.* Microtubule-Binding R3 Fragment from Tau Self-Assembles into Giant Multistranded Amyloid Ribbons. *Angew. Chemie - Int. Ed.* **55**, 618–622 (2016).
8. Pomerantz, W. C. *et al.* Nanofibers and lyotropic liquid crystals from a class of self-assembling  $\beta$ -peptides. *Angew. Chemie - Int. Ed.* **47**, 1241–1244 (2008).
9. Cui, H., Muraoka, T., Cheetham, A. G. & Stupp, S. I. Self-Assembly of Giant Peptide Nanobelts. *Nano Lett.* **9**, 945–951 (2009).
10. Calabrese, V. *et al.* Understanding heat driven gelation of anionic cellulose nanofibrils: Combining saturation transfer difference (STD) NMR, small angle X-ray scattering (SAXS) and rheology. *J. Colloid Interface Sci.* **535**, 205–213 (2019).
11. Cui, H., Cheetham, A. G., Pashuck, E. T. & Stupp, S. I. Amino acid sequence in constitutionally isomeric tetrapeptide amphiphiles dictates architecture of one-dimensional nanostructures. *J. Am. Chem. Soc.* **136**, 12461–12468 (2014).
12. Hule, R. A., Nagarkar, R. P., Hammouda, B., Schneider, J. P. & Pochan, D. J. Dependence of self-assembled peptide hydrogel network structure on local fibril nanostructure. *Macromolecules* **42**, 7137–7145 (2009).
13. Nagy-Smith, K. *et al.* Molecular, Local, and Network-Level Basis for the Enhanced Stiffness of Hydrogel Networks Formed from Coassembled Racemic Peptides: Predictions from Pauling and Corey. *ACS Cent. Sci.* **3**, 586–597 (2017).
14. Novelli, F. *et al.* Polymorphic Self-Organization of Lauroyl Peptide in Response to pH and Concentration. *Langmuir* **36**, 3941–3951 (2020).
15. Okesola, B. O. *et al.* Supramolecular Self-Assembly to Control Structural and Biological Properties of Multicomponent Hydrogels. *Chem. Mater.* **31**, 7883–7897 (2019).
16. Roberts, D., Rochas, C., Saiani, A. & Miller, A. F. Roberts Effect of Peptide and Guest Charge on the Structural, Mechanical.pdf. (2012).
17. Schmitt, J. *et al.* TEMPO-oxidised cellulose nanofibrils; Probing the mechanisms of gelation: Via small angle X-ray scattering. *Phys. Chem. Chem. Phys.* **20**, 16012–16020 (2018).
18. Yu, Z., Tantakitti, F., Palmer, L. C. & Stupp, S. I. Asymmetric Peptide Nanoribbons. *Nano Lett.* **16**, 6967–6974 (2016).
19. Zhang, S. *et al.* A self-assembly pathway to aligned monodomain gels. *Nat. Mater.* **9**, 594–601 (2010).
20. Draper, E. R. *et al.* Using Small-Angle Scattering and Contrast Matching to Understand Molecular Packing in Low Molecular Weight Gels. *Matter* **2**, 764–778 (2020).
21. Mallia, V. A. & Weiss, R. G. Structure-Property Comparison and Self-Assembly Studies of Molecular Gels Derived from (R)-12-Hydroxystearic Acid Derivatives as Low Molecular Mass Gelators. *ACS Symp. Ser.* **1296**, 227–243 (2018).
22. McAulay, K. *et al.* Isotopic Control over Self-Assembly in Supramolecular Gels. *Langmuir* **36**, 8626–8631 (2020).
23. Terech, P. & Maitra, U. Structural and rheological properties of aqueous viscoelastic solutions and gels of tripodal cholamide-based self-assembled supramolecules. *J. Phys. Chem. B* **112**, 13483–13492 (2008).
24. Stupp, S. I., Zha, R. H., Palmer, L. C., Cui, H. & Bitton, R. Self-assembly of biomolecular soft matter. *Faraday Discuss.* **166**, 9–30 (2013).
25. Wang, Y. *et al.* Polyamine-induced, chiral expression from liquid crystalline peptide nanofilaments to long-range ordered nanohelices. *Soft Matter* **15**, 4818–4826 (2019).
26. Cui, H. *et al.* Spontaneous and X-ray-Triggered Crystallization at Long Range in Self-Assembling Filament Networks. *Science (80-. )*. **327**, 555–560 (2010).
27. Palmer, L. C. *et al.* Long-range ordering of highly charged self-assembled nanofilaments. *J. Am. Chem. Soc.* **136**, 14377–14380 (2014).
28. Gobeaux, F. *et al.* Structural role of counterions adsorbed on self-assembled peptide nanotubes. *J. Am. Chem. Soc.* **134**, 723–733 (2012).
29. Zhang, S. *et al.* A self-assembly pathway to aligned monodomain gels. *Nat. Mater.* **9**, 594–601 (2010).

30. Weingarten, A. S. *et al.* Self-assembling hydrogel scaffolds for photocatalytic hydrogen production. *Nat. Chem.* **6**, 964–970 (2014).
31. Gardel, M. L. *et al.* Elastic behavior of cross-linked and bundled actin networks. *Science* (80-. ). **304**, 1301–1305 (2004).
32. Wong, G. C. L. *et al.* Lamellar Phase of Stacked Two-Dimensional Rafts of Actin Filaments. *Phys. Rev. Lett.* **91**, 1–4 (2003).
33. Pelletier, O. *et al.* Structure of actin cross-linked with [formula presented]-actinin: A network of bundles. *Phys. Rev. Lett.* **91**, 3–6 (2003).
34. Liu, R. *et al.* “Nano-Fishnet” Structure Making Silk Fibers Tougher. *Adv. Funct. Mater.* **26**, 5534–5541 (2016).
35. Kim, U. J. *et al.* Structure and properties of silk hydrogels. *Biomacromolecules* **5**, 786–792 (2004).
36. Fink, T. D. & Zha, R. H. Silk and Silk-Like Supramolecular Materials. *Macromol. Rapid Commun.* **39**, 1–17 (2018).
37. Rathore, O. & Sogah, D. Y. Nanostructure formation through  $\beta$ -sheet self-assembly in silk-based materials. *Macromolecules* **34**, 1477–1486 (2001).
38. Smeenk, J. M. *et al.* Fibril formation by triblock copolymers of silklike  $\beta$ -sheet polypeptides and poly(ethylene glycol). *Macromolecules* **39**, 2989–2997 (2006).
39. SasView. SasView 3.1.2 Documentation. Available at: [https://www.sasview.org/docs/old\\_docs/3.1.2/index.html](https://www.sasview.org/docs/old_docs/3.1.2/index.html). (Accessed: 15th November 2022)
40. Baccile, N. *et al.* Self-Assembly Mechanism of pH-Responsive Glycolipids: Micelles, Fibers, Vesicles, and Bilayers. *Langmuir* **32**, 10881–10894 (2016).
41. Qiao, Y. *et al.* Metal-Driven Hierarchical Self-Assembled One-Dimensional Nanohelices. *Nano Lett.* **9**, 4500–4504 (2009).
42. Oda, R., Artzner, F., Laguerre, M. & Huc, I. Molecular structure of self-assembled chiral nanoribbons and nanotubes revealed in the hydrated state. *J. Am. Chem. Soc.* **130**, 14705–14712 (2008).
43. Lis, L. J., Quinn, P. J. & Collins, J. M. Structures and Mechanisms of Phase Transitions in Surfactant Mixtures: Systems Which Induce the Ribbon Phase. *Mol. Cryst. Liq. Cryst. Inc. Nonlinear Opt.* **170**, 119–133 (1989).
44. Hyde, S. T. Identification of Lyotropic Liquid Crystalline Mesophases. in *Handbook of Applied Surface and Colloid Chemistry*. (ed. Holmberg, K.) 299 (John Wiley & Sons, Ltd, 2001). doi:10.1002/asna.18730821002
45. Cuvier, A.-S. S. *et al.* pH-triggered formation of nanoribbons from yeast-derived glycolipid biosurfactants. *Soft Matter* **10**, 3950–3959 (2014).
46. Masuda, M. & Shimizu, T. Lipid nanotubes and microtubes: Experimental evidence for unsymmetrical monolayer membrane formation from unsymmetrical bolaamphiphiles. *Langmuir* **20**, 5969–5977 (2004).
47. Baccile, N. *et al.* Palmitic Acid Sophorolipid Biosurfactant: From Self-Assembled Fibrillar Network (SAFIN) To Hydrogels with Fast Recovery. *Philos. Trans. A* **379**, 20200343 (2021).
48. Greaves, T. L. *et al.* How ionic species structure influences phase structure and transitions from protic ionic liquids to liquid crystals to crystals. *Faraday Discuss.* **206**, 29–48 (2018).
49. Mannock, D. A. *et al.* The thermotropic phase behaviour and phase structure of a homologous series of racemic  $\beta$ -d-galactosyl dialkylglycerols studied by differential scanning calorimetry and X-ray diffraction. *Chem. Phys. Lipids* **148**, 26–50 (2007).